UNIVERSITY OF CALIFORNIA
RIVERSIDE

Laser Energy Interaction With Novel Fine-Grained Materials

A Dissertation submitted in partial satisfaction
of the requirements for the degree of

Doctor of Philosophy

in

Mechanical Engineering

by

Kendrick Mensink

June 2019

Dissertation Committee:
Dr. Suveen Mathaudhu, Co-Chairperson
Dr. Guillermo Aguilar, Co-Chairperson
Dr. Lorenzo Mangolini

The Dissertation of Kendrick Mensink is approved:

_____

_____

Committee Co-Chairperson

_____

Committee Co-Chairperson

University of California, Riverside

Acknowledgements

The text of this dissertation, in part, is a reprint of the material as it appears in the Journal of Materials Processing Technology, 2018, “High repetition rate femtosecond laser heat accumulation and ablation thresholds in cobalt-binder and binderless tungsten carbides”. This reprint is contained in chapter two. The co-authors Guillermo Aguilar and Suveen Mathaudhu listed in that publication directed and supervised the research which forms the basis for this dissertation. The co-authors Elias Penilla, Pablo Martínez-Torres, and Natanael Cuando assisted by densifying and providing samples (EP), measuring thermal properties (PMT), and modeling heat accumulation (NC).

For chapter one the authors acknowledge the use of shared facilities at the UCR Center for Nanoscale Science and Engineering (CNSE), the Center for Advanced Microscopy and Microanalysis (CFAMM), and the Analytical Chemistry Instrumentation Facility (ACIF [NSF CHE-9709036]). The authors are also grateful to Christian Roach for his help with SEM and Xinzhu Zheng for her help with mechanical characterization. We also thank Dr. Javier Garay for use of his shared laser equipment and Dr. Juan Hernández for productive discussions and comments. KM acknowledges the support of the Department of Education Graduate Assistance in Areas of National Need (GAANN). SM acknowledges the support of UC Riverside research start-up funds. GA acknowledges the partial financial support of the National Science Foundation and AFOSR/CICESE.

For chapter two the authors acknowledge the use of shared facilities at the UCR Center for Advanced Microscopy and Microanalysis (CFAMM) and UCR Materials Science and Engineering (XRD). The authors are also grateful to UCR’s Matt McCormick for his help

machining the Hall flow funnel, Li-Ming Yeong for his help with milling sample preparation and flow analysis, Joshua Edwards and Jesus Rivera for their help with commercial prints, powder, and laser parameters, Thomas Dugger for his help with the heated stage, Taifeng Wang and Luz Cruz for their help with DSC/TGA, and David Kisailus for his generous shared equipment usage (commercial SS17-4PH powder, ProX DMP 200, heated stage). We also thank Noah Philips and ATI for providing commercial CoCr atomized powder, Dr. Allison Beese for providing early commercial powder, and Dr. Sandip Harimkar for testing low CO_2 laser power powder melt feasibility. KM acknowledges the support of the Department of Education Graduate Assistance in Areas of National Need (GAANN). SM acknowledges the support of UC Riverside research start-up funds.

Dedication

To my numerous family members, friends, and colleagues, which made this possible by supporting me in countless ways. I hope I support you as well as you support me.

ABSTRACT OF THE DISSERTATION

Laser Energy Interaction With Novel Fine-Grained Materials

by

Kendrick Mensink

Doctor of Philosophy, Graduate Program in Mechanical Engineering
University of California, Riverside, June 2019
Dr. Suveen Mathaudhu and Dr. Guillermo Aguilar, Co-Chairpersons

Laser irradiation is a unique technique used to process materials, it is “contactless”, rapid, and highly localized. The scope of this work is focused laser energy interacting with powdered materials that are in one case consolidated before, or in the second case, as a result of, laser irradiation.

Ultrafast laser pulses, pico and femtoseconds long, have provided new ways of processing materials due to either multiphoton absorption or lack of heat affected zones. However, pulsed laser incubation effects, in which the material is heated or ablated at lower laser energy density than expected, is not well understood. The first objective is to characterize the ultra-low laser density machining capability of a high repetition rate (55 MHz) femtosecond laser. The laser energy density ablation thresholds were found for several materials to be two orders of magnitude below single pulse thresholds. Results focus on fine-grained binderless tungsten carbide, which is ultrahard and difficult to

machine, especially without the metal binder phase. This relatively unexplored regime of laser ablation is found not ideal for precise machining of ultrahard materials due to the heat affected zones and relatively slow removal rates, however, it forecasts promising ultrafast laser micro-machinability at repetition rates below heat accumulation, which depends on the thermal relaxation time.

In the second case, more commonplace continuous wave laser heating is applied to loosely packed ball-milled metal powders to investigate their usefulness in additive manufacturing. The milled powders are compared to industry-standard atomized powders and are found to be feasibly additively manufactured in terms of size distribution, flowability, and potential grain boundary pinning precipitate benefits. However, questions remain regarding the sintered density and scalability to parts larger than laboratory test dimensions.

The findings forecast ideal repetition rates for ultrafast ablation to be hundreds of kHz, depending on thermal diffusion length and time constant, and that milled powder approaches for additive manufacturing are feasible and could help overcome some of the challenges related to alloy design and residual porosity in atomized powders.

Table of contents

List of Figures

List of Tables

Introduction Chapter

Introduction

1.1 Objectives

The overarching *research objective* of my dissertation is to uncover fundamental energy-matter interactions during laser processing of novel materials. Our fundamental understanding of laser-matter interaction will be improved through implementing laser processing in innovative ways or on unconventional materials. The results from these studies are aimed to broaden the scope of material processing via laser irradiation.

The broad objectives for the study include:

1) Explore the effect of femtosecond (fs) laser irradiation on the resultant ablation at ultra-low fluence, high repetition rate.

A few practical questions are addressed and tied to this objective. Is ultra-low fluence, high repetition rate fs laser irradiation useful for machining binderless tungsten carbide? Does this ultra-low fluence, high repetition rate fs laser irradiation exhibit selective removal of the binder phase of bindered tungsten carbide?

2) Explore effect of particle processing and microstructure on continuous wave (cw) laser coalescence.

Again, several questions are addressed and tied to this second objective. How can we design/test new additive manufacturing (AM) alloys? How can feedstock alloy powders be better tailored to the unique localized rapid thermal gradients of AM? Can milled AM feedstock powder be spread? What are the power density limits for joining?

Each objective should be understood in the context of related work in the fields of laser ablation and laser sintering. In addition, the materials structure pre- and post- processing should be characterized and compared to other processing techniques or mechanisms. The objectives each culminate in publications submitted in peer-reviewed journals and chapters in the dissertation.

1.2 Background

Laser processing of materials has been increasingly researched and utilized over the past half century (Bäuerle, 2011; Carpene et al., 2010; Singh, 1994). In the 1960s Ruby, Nd:YAG, CO_2, dye and other lasers were developed for the first time, and in the 1970s their reliability and durability improved. The 1980s and 1990s saw an exploration of these lasers for applications like cutting, welding, drilling and marking. While low power lasers became useful for communications, metrology, reprography and entertainment, high power lasers were used in weapons, chemical spectroscopy, deposition, medicine, scientific inquiry, and as a heat source for processes like forming, hardening and ablation. In 1982, the Ti:Sapphire laser was created, which introduced a new era of ultrashort femtosecond laser pulse scientific study. In 1984, the first 3D printed objects were created with a laser energy source.

Lasers are unique tools to process materials. They don't require masks like lithographic techniques, and they do not contact the material being processed, like a cutting tool would need to contact a workpiece to remove certain volumes. Lasers are very precise, localized, and highly controllable when used for material processing, and they can process virtually every material. The downsides are that laser typically only process

surfaces, they are typically expensive to obtain and maintain, they can be slow compared to other techniques, and often exhibit undesirable thermal and redeposition effects.

1.3 Selected emerging laser research fields

1.3.1 Ultrafast laser ablation threshold

There are several emerging areas of laser processing research relevant to this project that are developing in tandem with laser technology advances and greater availability of affordable turnkey laser systems. The first area is ultrafast laser ablation. Laser ablation phenomena has typically been divided categorically by the electronic structure of the target material: metals (metallic bonding and no bandgap), semiconductors (covalent bonding and small bandgap) and dielectrics (ionic and covalent bonding and large bandgap, $E_g > h\nu$). The main difference being the mechanism of absorption and thermal properties. Multiphoton absorption becomes an important mechanism for ablation of dielectrics if temperature related phenomena are not responsible. In addition, the thermal diffusivity and geometry of the material, along with pulse length and repetition rate, will determine the width of the heat affected zone (HAZ) and whether heat will accumulate between pulses.

Laser ablation has been studied to understand the effect of polarization, repetition rate, fluence, energy per pulse, wavelength, and pulse length. For example, nanosecond pulses with relatively large fluences exhibit high removal rate via melt ejection but cause resolidified melt crowns and heat affected zones (HAZ) near the ablation volume (Leitz et al., 2011). In contrast, femtosecond pulses with sufficient fluence for single pulse ablation exhibit higher precision ablation edges without melting or HAZ. These ultrafast

pulses can drill high aspect ratio holes in almost any material with high precision and fast processing times. This is due to non-thermal heating, where the electrons absorb sufficient energy to delocalize before the lattice heats. One important physical "two temperature" model was previously developed with the study of electron emission from picosecond laser pulses by Anisimov et al., (1974). The model predicts separate electron and lattice (phonon) temperatures for times shorter than the characteristic time for transfer of energy (or electron relaxation) from laser-excited electrons to the lattice.

In recent efforts to increase material removal rate, higher average power, high repetition rate ultrafast lasers have been utilized (Ancona et al., 2009, 2008). However, heat accumulation pulse-to-pulse can cause melting, also known as incubation effects. The associated loss in precise laser drilling in several materials has again been a barrier to further high-power laser machining applications.

In somewhat related research, some have noticed a significant drop in the ablation threshold fluence when using multi-pulse ultrafast irradiation. The reasons for this drop are still not well understood, although some theories have been presented (Di Niso et al., 2013; Häfner et al., 2016; Mannion et al., 2004). This proposal's preliminary work has demonstrated ablation in several materials via femtosecond pulses at fluences well below the threshold for single pulse ablation. These pulses are fixed at a comparatively very high repetition rate of 55 MHz, which is speculated to cause ablation after a few hundred milliseconds of exposure in a quasi-continuous wave melt ejection mechanism. The heat generated by each pulse does not have time to dissipate away from the interaction volume before the next pulse arrives ~18 nanoseconds later. The heat accumulation ablation

mechanism is supported by the presence of resolidified melt crowns around the ablation volume and analytical models (Finger and Reininghaus, 2014; Weber et al., 2014). As far as we have found, no publications have been written explicitly on the sub-category of ultra-low fluence or ultra-low energy per pulse ablation.

1.3.2 Additive manufacturing of metals

Although it is decades beyond initial invention, additive manufacturing is one of the most intensely researched areas related to laser material processing over the past several years due to the idea of fast, low waste, customizable, complex part fabrication. Laser-induced structural transformations such as melting, sintering and annealing processes in additive manufacturing are based on the high processing temperatures that can be reached during short heating and cooling cycles under high-power pulsed-laser or rapidly scanned cw-laser irradiation. In the case of surface absorption, which is a good approximation with metal applications, the thickness of the heated zone is approximately described by the heat-diffusion length, l_T. The time for heating the material to a certain temperature and depth, and the time for cooling can both be calculated, see chapter 6-9 of (Bäuerle, 2011). The thickness of the modified layer, $\Delta h \approx l_T$, decreases with decreasing pulse length. Ultrashort pulses can produce cooling rates up to 10^{12} K/s while fine grain or glass formation in metals requires cooling rates of 10^6-10^{12} K/s. Typical critical liquid-solid interface velocities are 10^2-10^3 m/s to avoid coarse grain structure. Non-equilibrium phases can be frozen and nucleation processes can be suppressed above or below melting. Thermally induced contraction cracks and melt spheroidisation are common problems mitigated by pre-heating the sample to reduce the thermal gradient. An overarching

limitation or benefit is the transformation temperature must be maintained long enough for the time required for phase transformation to occur.

Bulk nanocrystalline material produced through additive manufacturing has not been very well explored. Laser processing that produces nanocrystalline surface layer has been explored via laser shock processing (Liao et al., 2016), laser deposition (Lin et al., 2012), and direct surface nanostructuring (Veiko and Konov, 2014). Top down approaches to nanocrystalline material can be quite challenging and bottom up approaches have geometric shape limitations or require extra post consolidation machining to achieve a desired complex shape. There remains a large potential to create bulk nanocrystalline parts from alloys tailored to rapid densification via laser or other localized sintering techniques.

1.3.3 Importance of fine grain structure

The initial structure and properties of the target materials plays a significant role in the effect of ultrafast or continuous wave laser irradiation on the material. The materials have properties, either before or after laser processing, and often both, that make them more desirable for usage in industry and research. Perhaps the most significant material properties are strength and wear resistance (Zhao et al., 2019) in the case of laser joining alloyed particles in AM and high temperature stability and hardness (Fang et al., 2009) in the case of tungsten carbide. For both cases, the key is an initial nanostructured material. Nano or ultrafine grains, in combination with low porosity densification and a nano-precipitate phase, allow a cobalt chromium alloy to exhibit superior wear resistance. Nanocrystalline grains, in combination with certain supersaturated solid solution metal

alloys, allow for accelerated phase-separation sintering that maintain nearly the same grain size during pressureless laser heating (Park and Schuh, 2015).

Literature Review

2.1 Research related to ultrahigh repetition rate, ultra-low fluence femtosecond laser ablation

Heat accumulation or multi-pulse ablation threshold lowering has been observed in fused silica at 1 kHz with only 50 pulses (Lenzner et al., 1999), stainless steel at >500 kHz with only about 60 pulses (Ancona et al., 2008), stainless steel between 50 and 1000 kHz (Ancona et al., 2008), and shown not to occur in copper due to its high thermal conductivity except for possible model results above four MHz (Schille et al., 2010). Heat accumulation was evident in CrNi-steel between 85 and 125 kHz (Weber et al., 2014). These observations were made above the single pulse ablation threshold. There remains doubt about the cause of multi-pulse ablation threshold lowering and accompanying physical models. It may be increased absorption at higher temperatures due to oxidation (Neuenschwander et al., 2013) or defect states in the bandgap of dielectrics and semiconductors (Bäuerle, 2011, chap. 12.8.2), and/or multi-photon absorption. The trend of publications in high repetition rate ultrashort laser ablation is that higher average powers are being explored for faster material removal rates (Neuenschwander et al., 2014), but particle/plasma shielding, HAZ, and melting are limiting factors. These factors have been overcome with some success by trepan drilling instead of fixed location percussion drilling (Jahns et al., 2013).

In the context of oxide formation, there is at least one report of similarly ultra-low fluence, high repetition rate femtosecond laser ablation by Cano-Lara et al., (2011). Ablation was observed in 500 nm Mo thin films with 60 fs, 6.5 nJ, 800 nm, 70 MHz laser pulses focused down to 3 x 5 μm elliptical spot diameters. Thermal incubation effects were attributed for ablation threshold about ¼ of that previously reported for Mo. Veiko and Konov, (2014) states that average intensities on the order of 10^{14} W/cm^2 exceed the ionization and ablation thresholds for any material. This preliminary experimental work has been limited to <1.2x10^{11} W/cm^2 peak intensity, and so material ionization is not possible.

In summary, the opportunity exists to directly study heat accumulation below the single-pulse ablation threshold in all types of materials. Akin to Schille et al., (2010), the role of thermal properties in relation to lattice thermal relaxation should be studied in materials with thermal conductivities between copper and steel. As ultra-high repetition rate lasers are becoming more affordable and finding increased usage in a variety of applications, the ability for simultaneous non-linear optical processing and predictable controlled temperature accumulation should be forecast.

2.2 Research related to accelerated laser sintering of thermally stable nanocrystalline binary alloys

Laser-induced structural transformations such as transformation hardening, annealing, recrystallization, glazing, shock hardening, polishing (planarization) and sintering, are based on the high processing temperatures that can be reached during short heating and cooling cycles under high-power pulsed-laser or rapidly scanned cw-laser irradiation.

Short processing cycles permit material transformations within thin films and surfaces without considerable influence on the substrate or the underlying bulk material. In the case of surface absorption, which is a good approximation with metal applications, the thickness of the heated zone is approximately described by the heat-diffusion length, l_T. The time for heating the material to a certain temperature and depth, and the time for cooling can both be calculated from the equations in Chapters 6-9 of Bäuerle, (2011). The thickness of the modified layer, $\Delta h \approx l_T$, decreases with decreasing pulse length. Ultrashort pulses can produce cooling rates up to 10^{12} K/s while fine grain or glass formation in metals requires cooling rates of 10^6-10^{12} K/s. Typical critical liquid-solid interface velocities are 10^2-10^3 m/s to avoid coarse grain structure. Non-equilibrium phases can be frozen and nucleation processes can be suppressed above or below melting. Thermally gradient-induced cracks and melt spheroidisation are common problems mitigated by pre-heating. The limitation is the transformation temperature must be maintained long enough for the time required for phase transformation to occur.

2.2.1 Demonstration of accelerated nano phase-separation sintering

Conventionally there has been a tradeoff when sintering nanocrystalline material, longer time at elevated temperature decreases porosity but also causes grain growth and loss of the improved NC properties like strength. Park and Schuh, (2015) demonstrated a significantly accelerated sintering mechanism that occurs in certain alloys that are prepared in supersaturated solid solution. A solute phase separation occurs at activation energy (temperature) lower than is normally required for pressureless sintering. This solute segregation at nano and micro scale boundaries is thought to support rapid

diffusional transport. This accelerated sintering is promising for producing bulk nanocrystalline material because it lowers the time at elevated temperature typically required in pressureless or liquid-phase sintering. Because no melting is realized in the process, approximate grain size is maintained throughout the sintering process. Demonstration of ultrahigh thermal gradient laser sintering (>1000K/s heating and cooling) to near full density of binary alloys tailored to achieve accelerated sintering of metastable solute-segregated nano-structure would be highly significant to development of metal laser additive manufacturing. In addition, if the laser sintering is achieved below the melt temperature, such that as-milled nanometric grain size is preserved, a new method for developing bulk nanocrystalline material of any shape possible in powder-bed additive manufacturing will be realized. Beyond those milestones, but not necessarily only if they are passed, is the predicted (Atwater and Darling, 2012) possibility of thermodynamically (Chookajorn et al., 2012) thermally stabile grain size.

Summary of opportunity and findings

What has not been done before is to study incubation effects at very high repetition rates. The opportunity to explore high (55 MHz) repetition rate, ultra-low fluence fs laser irradiation has been taken and found to result in very low ablated volumes per pulse, heat accumulation to melting over five to fifty million pulses (0.1 to 1 second exposure times), and heat affected zones on the order of the spot size, ~15 microns. This category of laser parameters is not ideal for clean, fast laser ablation, but it may prove useful in niche applications wishing for localized laser annealing with or without multiphoton absorption processing.

In the second objective, what has not been done before is to offer an inexpensive high throughput approach to developing and testing new materials for AM. The opportunity to explore small batch high energy ball milled particles against their atomized counterparts has been taken and found to result in very similar flowability, coalesced density, coalesced layer thickness, although with different initial crystal size and phase fractions. This milling and laser joining in a cup approach should be validated for large, multilayer AM builds, but is promising to explore high throughput, non-equilibrium, meta-stable phase enhanced properties. It promotes tailoring of powder to the AM process rather than the more commonly study of tailoring the AM processing parameters to the final coalesced powder properties.

References

Ancona, A., Döring, S., Jauregui, C., Röser, F., Limpert, J., Nolte, S., Tünnermann, A., 2009. Femtosecond and picosecond laser drilling of metals at high repetition rates and average powers. Opt. Lett. 34, 3304–6. https://doi.org/10.1364/OL.34.003304

Ancona, A., Röser, F., Rademaker, K., Limpert, J., Nolte, S., Tünnermann, A., 2008. High speed laser drilling of metals using a high repetition rate, high average power ultrafast fiber CPA system. Opt. Express 16, 8958. https://doi.org/10.1364/OE.16.008958

Anisimov, S.I., Kapeliovich, B.L., Perel-man, T.L., 1974. Electron emission from metal surfaces exposed to ultrashort laser pulses. J. Exp. Theor. Phys. 66, 375–377.

Atwater, M., Darling, K., 2012. A Visual Library of Stability in Binary Metallic Systems : The Stabilization of Nanocrystalline Grain Size by Solute Addition : Part 1 80.

Bäuerle, D., 2011. Laser Processing and Chemistry. https://doi.org/10.1007/978-3-642-17613-5

Cano-Lara, M., Camacho-López, S., Esparza-García, A., Camacho-López, M.A., 2011. Laser-induced molybdenum oxide formation by low energy (nJ)-high repetition rate (MHz) femtosecond pulses. Opt. Mater. (Amst). 33, 1648–1653. https://doi.org/10.1016/j.optmat.2011.04.029

Carpene, E., Hoche, D., Schaaf, P., 2010. Laser Processing of Materials, Fundamentals, Applications and Developments. https://doi.org/10.1007/978-3-642-13281-0

Chookajorn, T., Murdoch, H.A., Schuh, C.A., 2012. Design of Stable Nanocrystalline Alloys. Science (80-.). 337, 951–954. https://doi.org/10.1126/science.1224737

Di Niso, F., Gaudiuso, C., Sibillano, T., Mezzapesa, F.P., Ancona, A., Lugarà, P.M., 2013. Influence of the repetition rate and pulse duration on the incubation effect in multiple-shots ultrafast laser ablation of steel. Phys. Procedia 41, 698–707. https://doi.org/10.1016/j.phpro.2013.03.136

Fang, Z.Z., Wang, X., Ryu, T., Hwang, K.S., Sohn, H.Y., 2009. Synthesis, sintering, and mechanical properties of nanocrystalline cemented tungsten carbide - A review. Int. J. Refract. Met. Hard Mater. 27, 288–299. https://doi.org/10.1016/j.ijrmhm.2008.07.011

Finger, J., Reininghaus, M., 2014. Effect of pulse to pulse interactions on ultra-short pulse laser drilling of steel with repetition rates up to 10 MHz. Opt. Express 22, 18790. https://doi.org/10.1364/OE.22.018790

Häfner, T., Heberle, J., Dobler, M., Schmidt, M., 2016. Influences on incubation in ps laser micromachining of steel alloys. J. Laser Appl. 28, 022605. https://doi.org/10.2351/1.4944445

Jahns, D., Kaszemeikat, T., Mueller, N., Ashkenasi, D., Dietrich, R., Eichler, H.J., 2013. Laser trepanning of stainless steel. Phys. Procedia 41, 630–635. https://doi.org/10.1016/j.phpro.2013.03.126

Leitz, K.H., Redlingshöer, B., Reg, Y., Otto, A., Schmidt, M., 2011. Metal ablation with short and ultrashort laser pulses. Phys. Procedia 12, 230–238. https://doi.org/10.1016/j.phpro.2011.03.128

Lenzner, M., Krüger, J., Kautek, W., Krausz, F., 1999. Incubation of laser ablation in fused silica with 5-fs pulses. Appl. Phys. A Mater. Sci. Process. 69, 465–466. https://doi.org/10.1007/s003390051034

Liao, Y., Ye, C., Cheng, G.J., 2016. [INVITED] A review: Warm laser shock peening and related laser processing technique. Opt. Laser Technol. 78, 15–24. https://doi.org/10.1016/j.optlastec.2015.09.014

Lin, D., Suslov, S., Ye, C., Liao, Y., Liu, C.R., Cheng, G.J., 2012. Laser assisted embedding of nanoparticles into metallic materials. Appl. Surf. Sci. 258, 2289–2296. https://doi.org/10.1016/j.apsusc.2011.09.132

Mannion, P.T., Magee, J., Coyne, E., O'Connor, G.M., Glynn, T.J., 2004. The effect of damage accumulation behaviour on ablation thresholds and damage morphology in ultrafast laser micro-machining of common metals in air. Appl. Surf. Sci. 233, 275–287. https://doi.org/10.1016/j.apsusc.2004.03.229

Neuenschwander, B., Jaeggi, B., Schmid, M., Dommann, A., Neels, A., Bandi, T., Hennig, G., 2013. Factors controlling the incubation in the application of ps laser pulses on copper and iron surfaces 8607, 86070D. https://doi.org/10.1117/12.2004136

Neuenschwander, B., Jaeggi, B., Schmid, M., Hennig, G., 2014. Surface structuring with ultra-short laser pulses: Basics, limitations and needs for high throughput. Phys. Procedia 56, 1047–1058. https://doi.org/10.1016/j.phpro.2014.08.017

Park, M., Schuh, C.A., 2015. Accelerated sintering in phase-separating nanostructured alloys. Nat. Commun. 6, 1–6. https://doi.org/10.1038/ncomms7858

Schille, J., Ebert, R., Loeschner, U., Scully, P., Goddard, N., Exner, H., 2010. High repetition rate femtosecond laser processing of metals. Proc. SPIE - Int. Soc. Opt. Eng. 7589, 758915-758915–11. https://doi.org/10.1117/12.842600

Singh, J., 1994. Laser-beam and photon-assisted processed materials and their microstructures. J. Mater. Sci. 29, 5232–5258. https://doi.org/10.1007/BF01171533

Veiko, V.P., Konov, V.I., 2014. Fundamentals of Laser-Assisted Micro-and Nanotechnologies. Springer. https://doi.org/10.1007/978-3-319-05987-7

Weber, R., Graf, T., Berger, P., Onuseit, V., Wiedenmann, M., Freitag, C., Feuer, A., 2014. Heat accumulation during pulsed laser materials processing. Opt. Express 22, 11312. https://doi.org/10.1364/OE.22.011312

Zhao, C., Zhou, J., Mei, Q., Ren, F., 2019. Microstructure and dry sliding wear behavior of ultra fi ne-grained Co-30 at % Cr alloy at room and elevated temperatures. J. Alloys Compd. 770, 276–284. https://doi.org/10.1016/j.jallcom.2018.08.092

Chapter 1

High repetition rate femtosecond laser heat accumulation and ablation thresholds in cobalt-binder and binderless tungsten carbides

Kendrick Mensink,[a,b] Elías H. Penilla,[a,c] Pablo Martínez-Torres,[a,d] Natanael Cuando,[a,e] Suveen Mathaudhu,[a,f] and Guillermo Aguilar[a,g]

[a]*Department of Mechanical Engineering, University of California, Riverside, CA, 92521, USA*

[b] *kmensink@engr.ucr.edu*

[c] *epenilla@eng.ucsd.edu*

[d] *ptorres80@gmail.com*

[e]*natanael.cuando@gmail.com*

[f] *smathaudhu@engr.ucr.edu, co-corresponding author*

[g] *gaguilar@engr.ucr.edu, co-corresponding author*

Abstract: Femtosecond (fs) laser ablation has been studied for the potential of fast, high precision machining of difficult-to-machine materials like binderless tungsten carbide. Obstacles that have limited its efficiency include melting from heat accumulation (HA), particle shielding, and plasma shielding. To address HA without shielding effects, high repetition rate (54.7 MHz), ultra-low fluence fs laser irradiation is performed to study the incubation effect and subsequent HA-ablation threshold of fine-grained tungsten carbides. Exposure times on the order of 100 milliseconds were conducted in air with fluences (1.82 to 9.09 mJ/cm^2) two orders of magnitude below the single fs pulse ablation thresholds reported in literature (0.4 J/cm^2). Heat accumulation at high repetition rate

explains the ultra-low fluence melt threshold behavior resulting in melt crowns around ablated holes and grooves. The results of this study aid in predicting heat buildup in high repetition rate laser irradiation for applications that wish to achieve high ablation rates of difficult-to-machine, ultrahard materials and help enable shaping of binderless tungsten carbide for use in applications too extreme for bindered tungsten carbide.

Introduction

Lasers are increasingly useful for a variety of materials processing techniques including marking, cutting, biocompatible surfacing, and other types of surface modification and micromachining. Among the main advantages of laser material processing are localized precision processing and fast processing times for creating surface features on the micrometer (μm) scale. Sugioka and Cheng (2014) have noted how femtosecond (fs) lasers in particular have revolutionized material processing in a variety of applications, in part due to the minimized heat affected zone when ablating or vaporizing many materials. Therefore, ultrashort pulsed lasers are good candidates for controlling the topologies and properties of select surfaces while not significantly affecting nearby material properties. Echlin et al. (2015) have shown them to be effective for fast, layer-by-layer ablation with minimal or no associated damage, while Farsari et al. (2007) have demonstrated four orders of magnitude increase in laser scribing speed of silicon carbide by using unamplified high repetition rate (50 MHz) compared to amplified kHz systems. Tungsten carbide (WC) is a high-density material that is used in armor piercing ammunition, cutting tools and applications requiring high hardness or high temperatures. To increase formability and toughness a metallic binder, frequently cobalt (Co), is used,

although at the expense of tool hardness. Despite binderless WC having superior performance to its bindered counterpart in high temperature, high pressure applications, binderless WC has been less studied than bindered WC because of its limited formability. Because both binderless WC and bindered WC are very hard relative to other cutting materials, Jahan et al. (2011) have shown wire electro-discharge machining (EDM) to be an effective tool for simple or complex shaping of WC. With EDM however, complex shapes require complex dies, and electrodes are required regardless of the geometric complexity. For hard polycrystalline materials that are not amenable to photolithographic machining approaches, laser machining is one of very few techniques to remove small volumes at less than 50 μm resolution and with fast material removal rates. Thus Eberle and Wegener (2014) explored picosecond (ps) and nanosecond (ns) laser machining of WC and diamond, as an alternative method to EDM. EDM has limitations of electrode wear, machining only conductive samples and complicated sample fixturing within dielectric medium. A further benefit of fs laser processing is some unique surface morphology control. Dumitru et al. (2002) have shown that fs laser processing near the ablation threshold can produce surface ripples on ultrahard materials, including WC, which is of interest for tribological applications. Dumitru et al. also measured for the first time the ablation threshold of bindered WC to be approximately 0.4 J/cm^2. After Dumitru et al.'s measurement, Byskov-Nielsen et al. (2010) also measured the single pulse ablation threshold for various materials and found tungsten (W) to have nearly the same threshold as Dumitru's bindered WC: 0.44 ± 0.02 J/cm^2. Developing effective techniques to machine binderless WC will broaden its use in many binder-caustic or extreme

environment applications where bindered WC is currently used with limitations or unable to be used.

Femtosecond laser machining is a complex process that typically involves several mechanisms occurring across several timescales. The thermalization of absorbed fs laser energy and the mechanisms and timescales involved have been explained by von der Linde et al. (1997). A description of the mechanisms and corresponding two-temperature models were first reported in the literature by Anisimov et al. (1974) and then expanded upon by Nolte et al. (1997) as well as by Chen et al. (Chen et al., 2006), among others. However, several researchers have noticed a decrease in the ablation threshold, or an incubation effect, when studying multi-pulse fs ablation, for example of Mo thin films at 70 MHz (Cano-Lara et al., 2011) and stainless steel at 50-1000 kHz (Di Niso et al., 2014). Several reasons related to increased absorption due to structural defects (Neuenschwander et al., 2013) or surface roughness (Häfner et al., 2016) have been proposed, although few have studied incubation effects at MHz repetition rates. In addition to increased absorption, material thermal properties are known to vary with increasing temperature, although most models have assumed material properties to be constant. While it is difficult to probe *in-situ* temperature rise due to absorption of laser irradiation, irradiating well below the single pulse ablation threshold somewhat simplifies the processing mechanisms in play by removing variables of heat lost via ablated material, particle shielding, vaporization, plasma generation and the associated increase in absorption.

In many difficult-to-machine materials, such as WC, it is useful to know the minimum fluence at which ablation occurs so that non-ablative processes stay below that fluence threshold or so that texturing or machining-type processes stay above that threshold. Pfeiffer et al. (2011) measured the WC ablation threshold (0.38 J/cm^2) and determined the absorption coefficient to be $4.43 \cdot 10^5$ cm^{-1}. Surface roughness could be high enough to alter the reflectivity and absorption, however, to our knowledge none have reported ablation thresholds as a function of initial surface roughness. In addition, there have been reports that a WC binder phase may have a different ablation threshold than the WC phase. Pham et al. (2013) drilled holes in cemented (or bindered) tungsten carbide (cobalt carbide) with fs laser pulses and noted the formation of pores on the side walls of the holes suggesting the preferential removal of cobalt during fs laser drilling. Dumitru et al. also claimed cobalt binder was ablated before WC particles due to its lower melting temperature, however no other systematic studies on the effect of cobalt binders on ablation threshold have been reported.

Beyond the effects of surface roughness and the presence of metal binders in WC on the ablation threshold, the microstructure may influence laser ablation dynamics. For fluences well above the single pulse ablation threshold, phase boundaries and voids may influence the ablated particle size and morphology. However, for ablation well below the single pulse threshold, grain size may affect thermal diffusivity and conductivity, which significantly affects heat accumulation (HA) at high repetition rate irradiation. Perecherla and Williams (1988) reported that higher binder content, between 1.5 and 30 wt% Co, in bindered WC lowers thermal conductivity, from about 90 to about 45 W$\cdot$m^{-1}K^{-1}, due to

electron and phonon scattering by carbon (C) and W atoms presumably in solid solution in the binder phase. Upadhyaya (2001) and Wang et al. (2015) further confirmed this trend and Wang et al. found thermal conductivity in Co-bindered WC to increase with grain size from 1.5 to 9 μm range. Perecherla and Williams using different techniques showed thermal conductivity to increase with grain sizes in the 1.2 to 5.5 μm range at room temperature, which is due to fewer grain boundaries scattering phonons. While the literature reports do not present a full perspective of the complex microstructural effects on ablations thresholds, it can be generally deduced that defects which affect thermal conductivity will thereby also affect heat accumulation in high repetition rate laser irradiation.

To explore the machinability of binderless WC via laser micromachining as compared to Co-bindered WC, we report on the ablation behavior of these materials under high repetition rate, ultra-low-fluence fs laser irradiation. HA-ablation spots developed after milliseconds (ms) of laser exposure on polished, fine-grained binderless and Co-binder WC materials. A better understanding of the ablation mechanisms and incubation effects at these irradiation conditions and sample microstructures will help forecast the feasibility of using ultrafast laser processing for relatively precise and fast machining of WC while avoiding shielding effects and multi-pulse heat accumulation. It will also help forecast the ability to replace bindered WC with binderless counterparts in more demanding environments.

Methods

2.1: Material preparation

Binderless WC samples were densified with Current Activated Pressure Assisted Densification (CAPAD), a process previously described extensively in (Garay, 2010). This technique allows the consolidation of near unity relative density bulk materials at low temperatures, enabling the production of fine grained binderless WC, which cannot be made with traditional free-sintering, or liquid-phase sintering approaches. For this study, commercially available binderless WC powder (TaeguTac, 99.95% purity, 500 nm grain size) samples were prepared. Each sample was heated at 300 °C/min until reaching hold temperature, and then held for 300 s at the maximum temperature. To vary relative density (void fraction), hold temperatures of 1400, 1500, 1600, 1700 and 1800 °C were used. Throughout the heating cycle, a maximum pressure of 60 MPa was uniaxially applied. After densification, the samples were mechanically polished using silicon carbide paper (600, 800, 1200 grit) and suspended alumina particles (9, 1, 0.05 μm). Commercially available (Ohio Carbon Blank, Columbus, OH) 800 nm grain size WC-10 wt% Co (hereafter "bindered" or WC-10Co) samples were also polished in the same steps. All samples were ~2 mm thick after polishing and 19 mm in diameter.

2.2: Irradiation conditions

The laser used for the experiments was an Amplitude Systems MIKAN Ytterbium doped Ti:Sapphire-based system delivering 230 fs pulses at a central wavelength of 1028 nm. The beam was focused perpendicular to the sample surface using an achromatic lens with a focal length of 18 mm. A Gaussian FWHM spot size diameter of 16 μm was used for

all experiments. The repetition rate of the laser was 54.7 MHz, measured by photodiode DC-coupled to a 1 MΩ oscilloscope. An electro-mechanical shutter was applied to get the desired exposure times; 0.10, 0.20, 0.50, 1.00, 2.00 and 5.00 s for these experiments (Fig. 2 and Fig. 3). A half waveplate and polarizer were used to attenuate the average laser power, which was set to 200, 300, 400, 500, 600, 700, 800, 900 and 1000 mW with a calibrated power meter. The pulse energy is derived by dividing the average power by the laser repetition rate. The resulting applied pulse energies used were 3.66, 5.48, 7.31, 9.14, 11.0, 12.8, 14.6, 16.5 and 18.3 nJ. Fluences were calculated as pulse energy divided by spot area, and were 1.82, 2.73, 3.64, 4.55, 5.46, 6.37, 7.27, 8.18 and 9.09 mJ/cm^2, respectively.

In addition to generating HA-ablation in fixed locations, microchannel grooves were machined using fluences near HA-ablation thresholds to study the effect of scanning speed on heat accumulation and machining morphology. Microchannel grooves were machined on the sample surfaces by translating the samples perpendicular to the beam at speeds of 0.10, 0.25, 0.50, 0.75 and 1.00 mm/s. Light microscopy images were taken of grooves irradiated over a length of 1000 μm (see Fig. 4) with 150 μm separation between the five parallel scanning speeds grooves.

Using a power meter to measure the reflected laser light after polishing, the binderless WC was measured to have approximately 36% reflectance and WC-10Co WC 35%. Reflectance measurements on samples polished with 600 and 800 grit silicon carbide paper enabled the verification of polishing to a sufficient and consistent level (1200 grit or 9 μm suspended alumina) to achieve mostly specular reflection. Diffuse reflection was

obvious in samples that were polished with 600 grit silicon carbide paper, which was the coarsest polish used in our sample preparation. The HA-ablation and micromachining experiments were conducted on samples that had been polished with 1 μm alumina particles suspended in felt with water to minimize surface roughness effects.

Light microscopy helped to qualify the surface finish and initial laser ablations. Scanning electron microscopy (SEM) was performed on a FEI NNS450 and was used to determine the areas of the HA-ablation and heat affected zones (Fig. 2). The height and depth of the ablated surface structures (Fig. 3) are found using an AIST-NT atomic force microscope (AFM). The groove profiles (Fig. 4) were measured using a Dektak profilometer with a 200-nm diamond tip. Hardness and fracture toughness from Vickers indentation, following Anstis et al. (1981) were obtained from a Nanovea mechanical tester. Thermal diffusivity (α) was found using photothermal radiometry, after Martínez-Torres et al., (2009), specific heat capacity (C_p) was measured using a thermogravimetric analysis-differential scanning calorimeter (TGA-DSC), and density (ρ) was found using Archimedes method; the product of these three gives thermal conductivity (k).

Results

3.1: Thermal and mechanical properties

The increased densification temperature has multiple effects on sample properties through control of the void fraction, or density relative to full theoretical density of 15.66 g/cm^3 (Page et al., 2008) (ICSD code 246149). As expected, increased density correlates with increased hardness, increased K_{IC} fracture toughness, and increased thermal diffusivity. Only WC densified at 1600, 1700, and 1800 °C (hereafter WC_{1600}, WC_{1700},

WC_{1800}) were judged to be of sufficient density to be used for laser irradiation testing. The thermal conductivity derived from the measurements in Fig. 1 are 52.9, 52.0 and 51.3 $W \cdot m^{-1}K^{-1}$ for WC_{1800}, WC_{1700} and WC_{1600}, respectively. Thermal conductivity of the commercial composite ceramic-metal WC-10Co follows a rule of mixtures between the binder and hard phase and although not measured, is expected to match typical commercial WC-Co conductivity values between 80 and 100 $W \cdot m^{-1}K^{-1}$.

Kim et al. (2006) also used field-assisted sintering (a process analogous in all but name to the CAPAD process) to produce binderless WC and reported 27.99 GPa Vickers hardness (10 kg_f) and 7.1 $MPa \cdot m^{1/2}$ fracture toughness, after Anstis et al. (1981), for 0.38 µm grain size. Bľanda et al. (2015) have studied the indentation hardness of the cemented WC constituents showing a significant influence of the crystallographic orientation of WC crystals, which, along with possible local void concentration under the indentation tip, increases the standard deviation error bars of hardness measurements in Fig. 1.

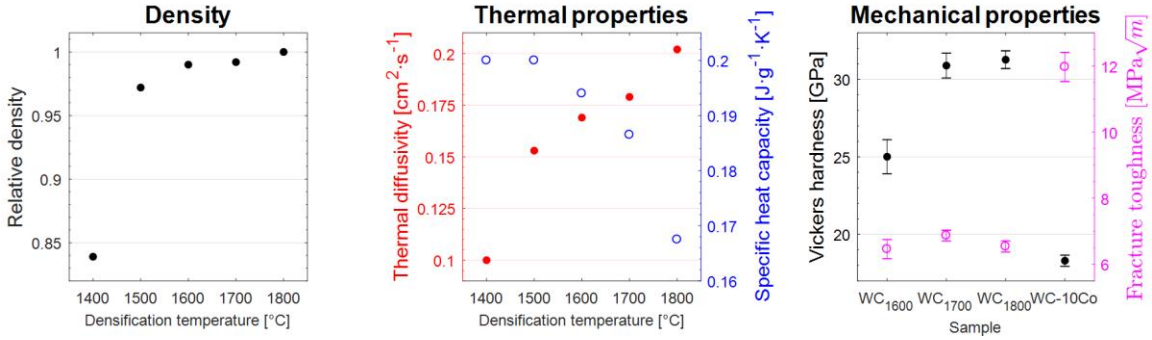

Fig. 1. Relative density (left), thermal diffusivity (center filled) and specific heat capacity (center open) of WC samples densified at 1400, 1500, 1600, 1700 and 1800 °C. Vickers hardness (right filled) and fracture toughness (right open) of WC samples densified at 1600, 1700 and 1800 °C compared to commercially available cemented WC-10Co. Error bars show standard deviation of twenty tests, otherwise data points represent a single measurement.

3.2: Heat accumulation-ablation spot characterization

In opaque materials, the lateral spot size dimensions (tens of μm) are commonly much longer than the optical penetration depth, (a few nanometers), primarily resulting in lateral diffusion of heat and ultimately generating a heat affected zone (HAZ) outward radially, as seen in Fig. 2. The threshold to develop a HAZ is evidently lower than HA-ablation and gives some insight of temperature distribution. HAZ threshold is observed with only microscopy, while the ablation zones are observable by microscopy and surface profilometry. Both types of areas are measured using SEM images with a brightness gradient filter fit to an ellipse. The fluence was varied by adjusting the laser power rather than by changing the spot size. The exposure times (left to right in Fig. 2) correspond to roughly 5.47, 10.9, 27.4, 54.7, 109 and 274 million pulses, respectively.

In all four samples (WC-10Co, WC_{1800}, WC_{1700}, WC_{1600}), spots irradiated less than 2.00 s with 2.73 mJ/cm^2 fluence do not exhibit ablated area clearly via SEM, but still have a HAZ. As shown by the blue filled data in Fig. 2, the HA-ablation threshold is crossed somewhere between 1.00 and 2.00 s of exposure at 2.73 mJ/cm^2 fluence for WC_{1700}. With SEM, WC_{1600}, WC_{1800} and WC-10Co also appear to cross the ablation threshold between 1.00 and 2.00 s of exposure at 2.73 mJ/cm^2, but other exposure time/threshold fluence combination thresholds are observed for the same samples and listed in Table 1. For example, from AFM the ablation threshold for WC_{1600} is between 0.10 and 0.50 s of exposure at 4.55 mJ/cm^2 fluence (Fig. 3) and for WC-10Co it is near 0.10 s of exposure at 3.64 mJ/cm^2 (not shown). Figure 2 shows the areas of the ablated spots and their

corresponding HAZ for WC_{1700} irradiated with fluences of 2.73, 4.55 and 9.09 mJ/cm^2 for exposure times between 0.10 and 5.00 s.

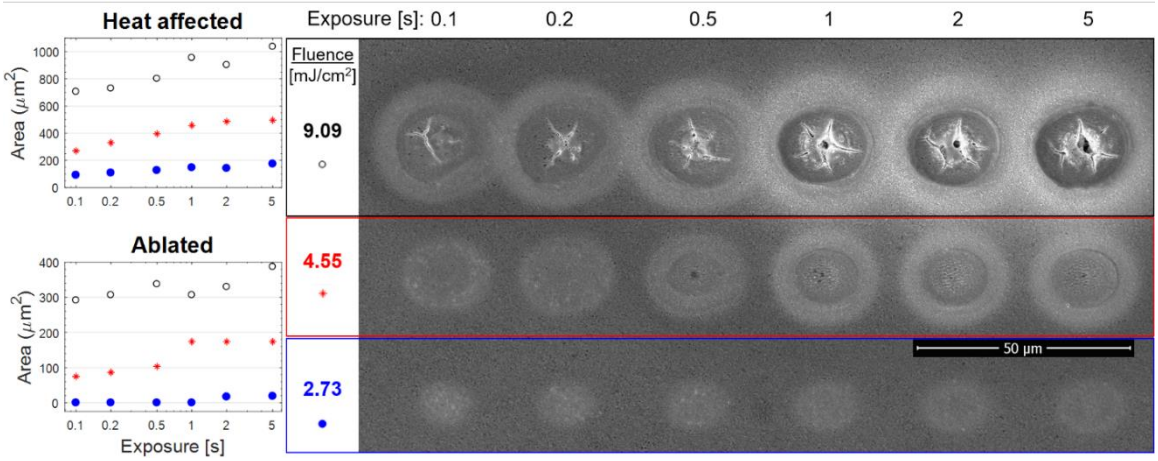

Fig. 2. WC_{1700} secondary electron SEM image and area measurements using a brightness gradient filter fit. Heat affected area (top left) includes any ablated area (bottom left) that developed inside the heat affected area. Fluences of 9.09 (black open), 4.55 (red asterisk) and 2.73 (blue filled) mJ/cm^2 are shown and measured for laser exposure times of 0.10, 0.20, 0.50, 1.00, 2.00 and 5.00 s.

Similar HA-ablation area behavior is observed between the three binderless WC samples, but the corresponding heat affected areas are largest on WC_{1600} and smallest on WC_{1800}, which is inversely related to the ordering of their thermal conductivities. We hypothesize that larger thermal conductivity results in larger heat dissipation and therefore smaller observed surface HAZ. WC-10Co HA-ablation areas are larger than the corresponding binderless WC areas at 2.73 mJ/cm^2 fluence, but generally smaller at 4.55 and 9.09 mJ/cm^2 fluences, while the crown area is generally larger. This may be related with the melting of the Co binder phase at a lower temperature (1495 °C) than the WC phase (2720 °C). Because thermal energy is dissipated faster in our WC-10Co sample, the HAZ is comparatively smaller, but at the lower threshold fluence of 2.73 mJ/cm^2 the melting

area is greater due to the presence of a lower melting point phase (10 wt% Co). However, at the higher fluences of 4.55 mJ/cm^2 a few non-mutually exclusive possibilities may help explain the smaller HA-ablation areas of bindered WC. One is that the WC phase melting begins to dominate, and another is that temperatures high enough to evaporate Co are reached (2925 °C), still another is that the binder phase, once melted, spreads to cover a larger fraction of the surface at the irradiation spot and reduces the absorption. Further studies that include chemical analysis should help clarify these possibilities. The WC-10Co sample did not crack at 9.09 mJ/cm^2 fluence for any exposure time up to 5 s. However, due to their lack of binder, lower toughness and higher hardness, all three binderless samples locally fracture at 0.50 s and longer exposures at 9.09 mJ/cm^2, as seen in the top row of Fig. 2.

Figure 3 shows the AFM height scans of the tungsten carbide surface after controlled exposure times. These spots correspond to experiments performed on the same sample surface as the experiments shown in Fig. 2. Note that the height is exaggerated to better show surface height variations in conjunction with a height color scale showing darker shades as lower and lighter shades as higher. The raised crown exhibited around all the spots irradiated above HA-ablation threshold is commonly seen in surfaces that have melted, typically from longer pulse length (ns) lasers. This raised ring suggests melting is occurring due to heat accumulation in our samples.

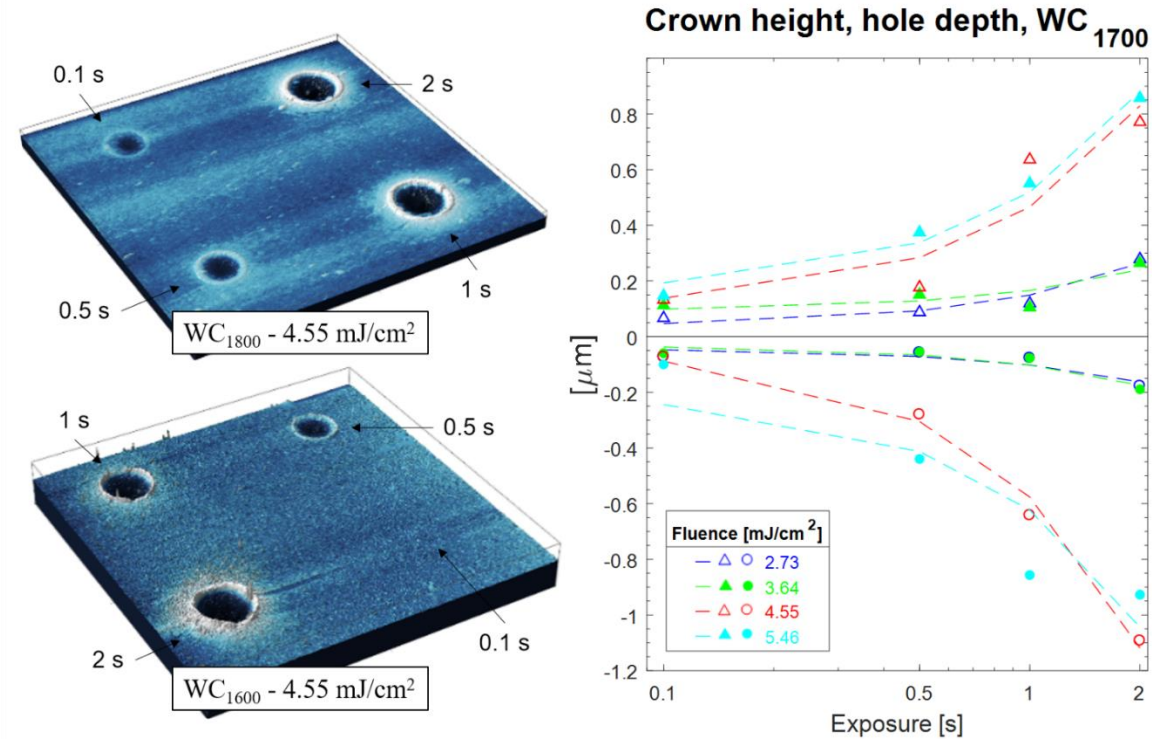

Fig. 3. AFM 3D representation of HA-ablation spots on binderless WC_{1800} (top left) and WC_{1600} (bottom left) with 4.55 mJ/cm^2 for 0.10, 0.50, 1.00 and 2.00 s exposure (height exaggerated). There is no crown or ablation evident in WC_{1600} or WC_{1700} after only 0.10 s of exposure at 4.55 mJ/cm^2 fluence. The height trends of WC_{1700} spots exhibiting crowns surrounding ablated volumes is plotted (right). Triangles show the highest points in each crown and circles show the lowest points in each hole for fluences of 2.73 (blue), 3.64 (green), 4.55 (red), and 5.46 (cyan) mJ/cm^2. Dashed trendlines are shown to help distinguish between overlapping data markers.

Among binderless WC, WC_{1800} with the highest thermal conductivity, has the most sensitivity to the exposure times required for HA-ablation: between 1.00 and 2.00 s at a fluence of 2.73 mJ/cm^2, 0.10 and 0.50 s at 3.64 mJ/cm^2 and less than 0.10 s at 4.55 mJ/cm^2. The WC_{1700} sample ablates between 1.00 and 2.00 s with a fluence of 2.73 mJ/cm^2. The WC_{1600} sample, with the lowest thermal conductivity of the binderless samples, ablates near 0.50 s at 2.73 and 3.64 mJ/cm^2 fluences, and between 0.10 and 0.50

s at 4.55 mJ/cm^2. This behavior perhaps expected in terms of thermal conductivity, but experiments with higher exposure time resolution would better elucidate the exposure time sensitivity behavior. Relative to the average height of the area immediately around the irradiation spot, we summarize the lowest point and highest point, wherever they may be, in each irradiated spot and crown area in the plot of Fig. 3. The AFM surface roughness on our polished samples hovers around 100 nm, which explains why even though there was no ablation observed on WC_{1700} after 0.10 s of exposure for fluences below 5.46 mJ/cm^2, there is still around 100 nm of crown height and hole depth plotted in Fig. 3. The WC-10Co sample crowns did not rise beyond 500 nm above the surrounding surface, which can be explained by the presence of Co evaporating away and/or helping to flow and flatten the semi-melted WC particles while molten. The hole depths of the WC-10Co matched the binderless WC samples in reaching around 1 μm depth at 2 s exposure but required 6.37 mJ/cm^2 fluence compared to 4.55 mJ/cm^2 for the three binderless samples.

3.3: Irradiated grooves characterization

The light microscopy surface morphology images, as seen in Fig. 4, show the difference between HA-ablation with (i.e. WC_{1700} with 8.64 mJ/cm^2 fluence at 0.10 mm/s scan speed) and without accompanied ejected debris along the groove edges. The cross-sectional width and shape of the laser-cut grooves is inconsistent between profilometry scans, likely due to a somewhat stuttered scanning velocity over time as the stepper motors jog from step to step during laser processing. Translation stages with more smooth velocity are expected to improve the groove profile consistency. Although

various profiles along the same sample at the same speed and fluence are not shown, their statistically varying widths, depths and roughness's are supported by what appears as overlapping spots in the binderless WC surface groove images shown in Fig. 4. The groove profiles shown in Fig. 4 were selected from at least five profiles of each sample to highlight a relatively ideal cutting cross section profile: high ablation to recast ratio, clean material removal in the groove, and high aspect ratio groove. In Fig. 4, the profile shown at 0.25 mm/s (red) is much wider than the other profiles shown due to the relatively large fluence (9.09 mJ/cm^2) and slow scan speed.

The cross-sectional area of the laser machined grooves (darker shade) and the melted recast peaks (lighter shade) was measured for the profiles in Fig. 4 and is reported to the right of each profile, highlighted for recast and boxed for ablated. Slower scan speeds and higher fluences yield larger HA-ablation to recast volume ratios.

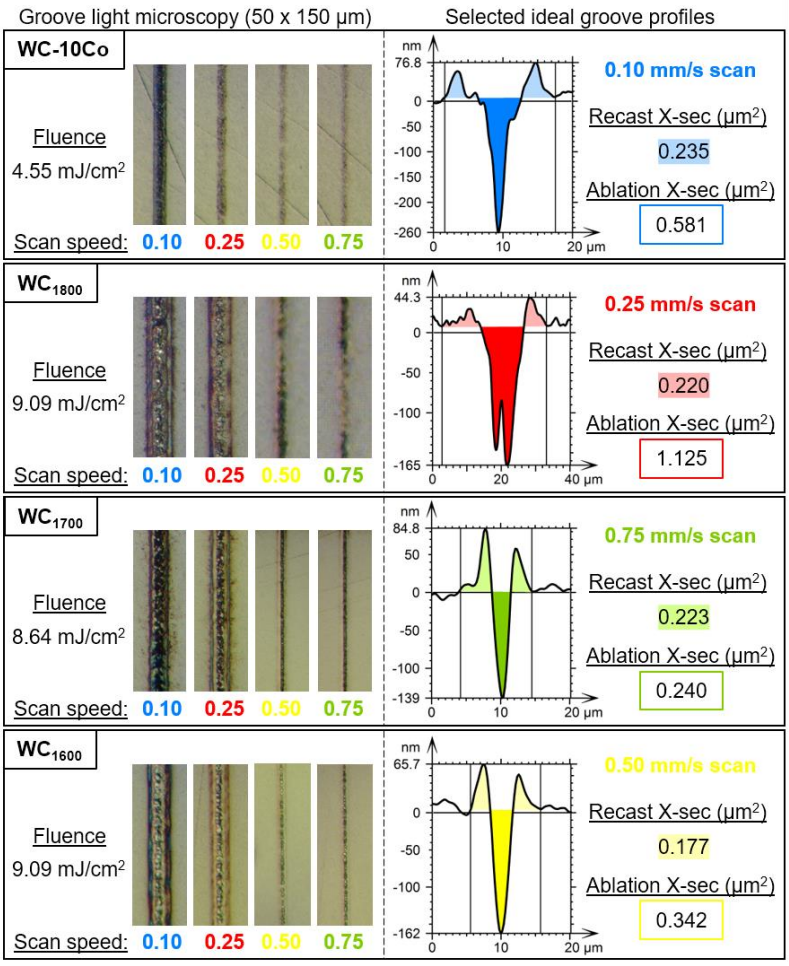

Fig. 4. Light microscopy images of the WC-10Co, WC_{1800}, WC_{1700} and WC_{1600} sample surfaces irradiated with the fluences labeled (left). Each sample has a selected groove profile shown (right), selected for high ablation volume and aspect ratio, at one of four color-coded scan speeds: 0.10 mm/s (blue), 0.25 mm/s (red), 0.50 mm/s (yellow), 0.75 mm/s (green). The profiles exhibit recast regions (lighter shade) on either side of the ablated groove (darker shade), which have cross sectional area reported to the right of the corresponding profile for both recast (highlighted) and ablated (boxed) areas. Note the z scale is in nm to show detail.

For the same scanning speeds, bindered WC exhibit about half the continuous groove HA-ablation threshold fluence (4.55 mJ/cm^2) of the binderless counterparts (9.09 mJ/cm^2). This is perhaps not expected when compared with the fixed-location HA-

ablation thresholds, but again explained by the presence and preferential melting ablation of the lower melting point binder phase. This hypothesis can be supported by our observation of the larger recast kerf cross section area of the WC-10Co sample when compared to the binderless WC samples at the same translation and fluence conditions. The higher CAPAD processing temperature of the binderless WC corresponds with slightly more ablated cross-sectional area at the same fluence and scanning speed. These results agree with the general observation that higher thermal conductivity samples exhibit HA-ablation at lower fluences when translating the samples. All the groove profiles ablation widths were less than or equal to the laser spot size while the recast widths could extend beyond the laser spot size up to about 10 μm radially.

Discussion

4.1: Context of multi-pulse laser ablation

Laser ablation can be categorized into thermal and nonthermal. Pulses longer than a ns typically cause absorbing samples to increase in thermal energy to melting temperature before significant ablation occurs through other mechanisms. With the development of ultrafast pulse systems, Liu et al (1997) and others found the HAZ could be reduced or even eliminated. Fujimoto et al. (1984) were early to report that electrons excited by pulses shorter than or equal to electron-phonon energy relaxation time are temporarily not in thermal equilibrium with the lattice. With sufficient energy, as in ultrafast single pulse ablation measurements, these nonequilibrium electrons lead to so-called nonthermal ablation mechanisms, which incidentally, is not observed in this study.

If fluence is above the single pulse ablation threshold, material ablated from the previous pulse will remove thermal energy along with the ablated particles, which complicates models trying to account for thermal effects. When fluence is below the single pulse ablation threshold, then there is a possibility for heat to accumulate from pulse-to-pulse in the material without removal via ablation. The condition for heat to accumulate is that the time for thermalized laser irradiation to diffuse out of the focal volume must be shorter than the pulse cycle time. With an ultrashort and MHz repetition rate laser pulse train below the nonthermal single pulse ablation threshold, we may often find that the time between pulses is shorter than the time to diffuse heat out of the focal volume and therefore that heat is accumulating in the lattice. If we use experimental values to help us estimate this thermal relaxation time, after Bejan (18.43)

$$\tau_{thermal} \approx {L_p^2}/{2\alpha} \quad (1)$$

where L_p is the thermal penetration length and α is the thermal diffusivity, we can estimate if we are accumulating heat. Using 10 μm for the penetration length, conservatively based on the maximum range of visible HAZ (heat is diffused much further than what is visible on SEM of surface) of Fig. 2 for WC_{1700}, and 0.18 cm^2/s diffusivity for WC densified at 1700 °C from Fig. 1, we get a relaxation time of 2.8 microseconds (μs). This relaxation time is much longer than the time between pulses of our laser system (1/54.7 MHz) of 18.3 ns, thereby supporting a heat accumulation effect between successive pulses. Furthermore, if τ was 2.8 μs for a given material, the transition from thermal diffusion to heat accumulation would occur near 360 kHz (1/2.8 μs).

Literature reports a few examples of ultrafast ablation thresholds below the single pulse ablation threshold with high repetition rates. It has been reported previously by Eaton et al. (2008) that there is a transition from thermal diffusion to heat accumulation with 300-700 fs pulses at about 500 kHz in borosilicate glass, which has a softening temperature of 985 °C. While a 54.7 MHz repetition rate, more than 10 times higher than the highest repetition rate examined by Eaton (5 MHz) may seem to be too high to measure HA over a few seconds of irradiation, WC materials have about 50 times the thermal conductivity of borosilicate glass, so heat is dissipated much faster. Eaton et al. demonstrated that HA in borosilicate glass, albeit in the context of waveguide writing, is influenced by repetition rate, pulse energy, changes in absorption and state, and scanning speed. Along with heat accumulation, significantly lower ablation thresholds, on the order of mJ/cm^2, have been reported recently with ultrafast multi-pulse irradiation. In a report where heat accumulation conditions are likely met, Cano-Lara et al. (2011) observed high repetition rate (70 MHz) laser ablation of 500 nm thin film molybdenum on a fused silica substrate to be about one-fourth the previously reported laser ablation threshold fluence. This was attributed to thermal incubation effects. Cano-Lara measured a ~30 mJ/cm^2 threshold on a thin film (800 nm, 60 fs, ~2.4 nJ pulses), which is one order of magnitude higher than reported in this work. It is evident that repetition rate, material thermal properties, and nonlinear effects may all play a role in the incubation effects reported. A list of WC materials in Table 1 shows the variance of irradiation conditions that have been reported to achieve some type of ultrafast laser ablation, though thermal and optical properties of each material would aid completeness.

Table 1. Laser parameters of ultrafast ablation threshold in tungsten carbide materials

		Irradiance parameters			Pulse parameters		
Material	Grain size	Fluence	Exposure time	Rep rate	Energy	Length	Ablation type
Binderless WC_{1600}[a]	0.5 µm	2.73 mJ/cm^2	~500 ms	54.7 MHz	5.48 nJ	230 fs	Heat accumulation
		3.64 mJ/cm^2	~500 ms	54.7 MHz	7.31 nJ	230 fs	Heat accumulation
		4.55 mJ/cm^2	100-500 ms	54.7 MHz	9.14 nJ	230 fs	Heat accumulation
		5.46 mJ/cm^2	<100 ms	54.7 MHz	11.0 nJ	230 fs	Heat accumulation
Binderless WC_{1700}[a]	0.5 µm	2.73 mJ/cm^2	1.00-2.00 s	54.7 MHz	5.48 nJ	230 fs	Heat accumulation
		3.64 mJ/cm^2	~500 ms	54.7 MHz	7.31 nJ	230 fs	Heat accumulation
		4.55 mJ/cm^2	100-500 ms	54.7 MHz	9.14 nJ	230 fs	Heat accumulation
		5.46 mJ/cm^2	<100 ms	54.7 MHz	11.0 nJ	230 fs	Heat accumulation
Binderless WC_{1800}[a]	0.5 µm	2.73 mJ/cm^2	1.00-2.00 s	54.7 MHz	5.48 nJ	230 fs	Heat accumulation
		3.64 mJ/cm^2	100-500 ms	54.7 MHz	7.31 nJ	230 fs	Heat accumulation
		4.55 mJ/cm^2	<100 ms	54.7 MHz	9.14 nJ	230 fs	Heat accumulation
WC-10Co[a]	0.8 µm	2.73 mJ/cm^2	100-500 ms	54.7 MHz	5.48 nJ	230 fs	Heat accumulation
		3.64 mJ/cm^2	~100 ms	54.7 MHz	7.31 nJ	230 fs	Heat accumulation
		4.55 mJ/cm^2	<100 ms	54.7 MHz	9.14 nJ	230 fs	Heat accumulation
WC-10Co[b]	0.5 µm	0.4 J/cm^2	150 fs	1 kHz	2.8-54 µJ	150 fs	Single pulse
WC-6Co[b]	1.5 µm	0.3 J/cm^2	150 fs	1 kHz	2.8-54 µJ	150 fs	Single pulse
WC (unspecified)[c]	-	0.38 J/cm^2	150 fs	1 kHz	8.8 µJ	150 fs	Single pulse

Table 1. [a]This work, [b](Dumitru et al., 2002) and [c](Pfeiffer et al., 2011).

4.2: Summary of ultra-low fluence, ultrafast, multi-pulse laser heat accumulation and ablation

In the current study, non-thermal melting is not likely as it requires peak pulse intensities near 10^{12} W/cm^2, as discussed by (Rethfeld et al., 2004), while our experiments were conducted at 10^{10} W/cm^2. Instead, incident photons excite focal volume electrons on the timescale of the laser pulse (a few hundred fs) through absorption. On the next larger

timescale, energy from recently excited electrons is transferred to the lattice (heating) a few ps after the pulse. The timescale of lattice heating due to electron-phonon collisions, as discussed by Rethfeld and others, is a few to tens of ps, and well within the temporal pulse spacing (10 ns to 1 μs for MHz laser systems). Keeping in mind the temporal pulse spacing of our system is 18.3 ns, the time for complete thermal relaxation of the lattice must be greater than 18.3 ns for heat to accumulate, which our experimentally estimated thermal relaxation time of 2.8 μs is. Next, upon reaching melt temperature after sufficient laser exposure time, rapid material expansion and electrons excited beyond the Fermi level by multiphoton absorption cause particles to vacate the surface in all directions, typically leaving ejected particle debris and recently solidified particles nearby as seen in Fig. 4. The relatively slow melting ablation process of ions and particles in various degrees of melt moving away from the center of expansion occurs on the timescale of a few hundred ms, but this last step occurs only once the lowest melting point material phase is near the melting temperature from multi-pulse heat accumulation. The time required for the lattice temperature to reach melting temperature significantly depends on the absorption, fluence and material thermal conductivity. For the irradiation conditions of Fig. 2 and Fig. 3, the time before HA-melting is observed is on the order of hundreds of ms.

4.3: Heat accumulation modeling

If the material thermal and optical properties, as well as the laser parameters are known, temperature profiles in space and time can be calculated from various models. So far there is not a suitable model to fully represent the experimental conditions of this study.

Nonetheless, as approximations to provide insight, several models were explored. The two-temperature model is a widely used approach for fs laser absorption and it uses separate electron and lattice heat conduction equations, which are coupled by the electron-phonon coupling constant. For example, Breitling et al. (2004) demonstrate that the two-temperature model gives good insight of the electron and lattice temperature rise at the ps and ns scales, estimating electron temperature rises on the order of thousands of K for typical single laser pulses of 1 ps or less. Although this model is useful for single pulse phenomena and promising for exploring incubation effects, to the best of our knowledge it has not yet been used in providing information about the laser-induced heating due to many successive ultrashort pulses.

A single temperature HA model proposed by Weber et. al (2014) estimates, with good experimental consistency in the case of drilling holes in CrNi-steel, the temperature HA due to multiple ultrashort pulses. Furthermore, in the case of 3D isotropic semi-infinite absorbing material, the HA is predicted to lead to a finite temperature with infinite number of pulses. Using material and laser values from this work (density = 15.66×10^{3} kg/m^{3}, specific heat capacity = 167 $J\cdot kg^{-1}\cdot K^{-1}$, thermal diffusivity = 2.00×10^{-5} m^{2}/s, reflectivity = 36%, repetition rate = 54.7 MHz) in the Weber model resulted in HA temperature increase convergence to 710 and 2362 °C for fluences of 2.73 and 9.09 mJ/cm^{2}, respectively. High repetition rate lasers are also referred to as quasi-continuous wave. As a contrast, a continuous wave laser-induced temperature model with the same average powers (300 and 1000 mW) used in the Weber model, irradiating on an isotropic semi-infinite absorbing material (Ready, 1971, eqn 3.17) results in steady state

temperatures of 82 and 276 °C for fluences of 2.73 and 9.09 mJ/cm^2, respectively. The temperatures calculated by means of these two models seem low compared to our experimental melting results, considering the 2720 °C melting point of tungsten carbide reported by Dumitru et al. (2002). A model that adequately describes HA temperature induced by high repetition rate, ultrafast, multi-pulse laser pulse trains below ablation and melting thresholds is imminent, and this model should give insight into the mechanisms that govern these unique laser processing conditions.

4.4: Outlook and future work

In addition to the parameters explored in this study (thermal conductivity, machining speeds and exposure time), other parameters can be altered, as experimental equipment allow, to understand their influence on ablation threshold and heat accumulation more fully in the ultra-low fluence, high repetition rate ablation regime. These include a broader range of material thermal conductivity, reflectivity/absorptivity, grain size, laser pulse length, wavelength and repetition rate. It is expected that further studies will help elucidate the fundamental mechanisms of incubation effects. Furthermore, quantification of laser micro-processing effects on materials such as WC is expected to lead to advances in tribological properties, surface appearance, wettability, or surface repair in a broad range of materials classes. To the best of our knowledge, the difference in heat accumulation due to multiphoton absorption versus single photon absorption has not been studied and may have unique applications in non-linear optics.

Conclusion

Through the application of MHz repetition rate, ultra-low fluence laser irradiation, we propose that laser ablation is achieved via melting from heat accumulation processes. This type of ultrafast ablation is different from non-thermal ultrafast single and multi-pulse ablation and different from thermal "slow" (non-ultrafast) single and multi-pulse melting-ablations. HA-ablation and micromachining at very low fluences and very low energies per pulse, yet at comparatively high repetition rates is demonstrated to be two orders of magnitude below non-thermal ultrafast single pulse ablation threshold fluence for similar materials. The crown and ridge structures formed around the irradiation spots and grooves, respectively, are likely due to recast melt expansion from heat accumulation during exposure to the high repetition rate pulse trains. With similar surface roughness, reflectance and grain size (800 nm with Co binder and 500 nm without binder), the Co bindered WC exhibited half the HA-ablation threshold fluence (4.55 mJ/cm^2) of its binderless counterparts (9.09 mJ/cm^2) while the samples were scanned at speeds between 0.10 and 1.00 mm/s. However, at lower fluence of 3.64 mJ/cm^2, if the samples and laser were not moving during exposure, they exhibited similar HA-ablation threshold between 100 and 500 ms of exposure. As expected, increased scanning speed reduced heat accumulation and resulted in less HA-ablation cross sectional area. Increased scanning speed also decreased ablation to recast cross sectional area ratio. Our results show preliminary evidence that small decreases in HA-ablation threshold correspond with increasing thermal conductivity (and the related density, hardness, and thermal diffusivity) for binderless WC. We hypothesize grain size affects HA-ablation only

insomuch as it affects thermal conductivity. For the binderless samples, the heat affected areas are largest on WC_{1600} and smallest on WC_{1800}, which is inversely related to the ordering of their thermal conductivities. A few non-mutually exclusive possibilities may help explain the difference in HA-ablation areas between bindered and binderless WC. One is that there is a transition between which phase dominates ablation morphology: Co binder (1495 ℃) to WC (2720 ℃), another is that temperatures high enough to evaporate Co are reached (2925 ℃), still another is that the binder phase, once melted, spreads to cover a larger fraction of the surface at the irradiation spot and reduces the absorption. Further studies that include chemical analysis and higher resolution exposure times should help clarify these possibilities. We hypothesize the lower melting point binder, Co, melts at lower fluence and is still well-adhered to nearby WC as it ablates, and results in lower recast crown heights. The presence and preferential removal of Co, also noticed by Pham (2013) near the single pulse ablation threshold, is responsible for HA-ablation morphology differences with the binderless WC counterpart. In general, this ultralow fluence, MHz repetition rate laser ablation is not ideal for precise machining of ultrahard materials due to the heat affected zones and relatively slow removal rates, however, it forecasts promising ultrafast laser micro-machinability of binderless WC for extreme environment applications at repetition rates below heat accumulation, which depend on the thermal relaxation time. The advantages of the micromachining approach used in this work would be for niche applications that desire localized surface recrystallization or surface plasmonic effects, or for bandgap materials that desire nonlinear interaction

simultaneous to localized annealing or melting, and finally for semiconductor materials surface geometry or defect concentration “fine-tuning”.

References

Anisimov, S.I., Kapeliovich, B.L., Perel-man, T.L., 1974. Electron emission from metal surfaces exposed to ultrashort laser pulses. J. Exp. Theor. Phys+. 66, 375–377.

Anstis, G.R., Chantikul, P., Lawn, B.R., Marshall, D.B., 1981. A Critical Evaluation of Indentation Techniques for Measuring Fracture Toughness: I, Direct Crack Measurements. J. Am. Ceram. Soc. 64, 533–538. https://doi.org/10.1111/j.1151-2916.1981.tb10320.x

Ashkenasi, D., Stoian, R., Rosenfeld, A., 2000. Single and multiple ultrashort laser pulse ablation threshold of Al2O3 (corundum) at different etch phases. Appl. Surf. Sci. 154, 40–46. https://doi.org/10.1016/S0169-4332(99)00433-X

Bejan, A. 1993. Heat transfer. New York: John Wiley & Sons.

Bľanda, M., Duszová, A., Csanádi, T., Hvizdoš, P., Lofaj, F., Dusza, J., 2015. Indentation hardness and fatigue of WC – Co composites. Int. J. Refract. Met. H. 49, 178–183. https://doi.org/10.1016/j.ijrmhm.2013.04.006

Breitling, D., Ruf, A., Dausinger, F., 2004. Fundamental aspects in machining of metals with short and ultrashort laser pulses, in: Herman, P.R., Fieret, J., Piqué, A., Okada, T., Bachmann, F. G., Hoving, W., Washio, K., Xu, X., Dubowski, J. J., Geohegan, D. B., Träger, F. (Eds.), Photon Processing in Microelectronics and Photonics III, Proc. of SPIE vol. 5339, Bellingham, WA, United States, pp. 49-63. https://doi.org/10.1117/12.541434

Byskov-Nielsen, J., Savolainen, J.M., Christensen, M.S., Balling, P., 2010. Ultra-short pulse laser ablation of metals: Threshold fluence, incubation coefficient and ablation rates. Appl. Phys. A-Mater. 101, 97–101. https://doi.org/10.1007/s00339-010-5766-1

Cano-Lara, M., Camacho-López, S., Esparza-García, a., Camacho-López, M. a., 2011. Laser-induced molybdenum oxide formation by low energy (nJ)–high repetition rate (MHz) femtosecond pulses. Opt. Mater. 33, 1648–1653. https://doi.org/10.1016/j.optmat.2011.04.029

Chen, J.K., Tzou, D.Y., Beraun, J.E., 2006. A semiclassical two-temperature model for ultrafast laser heating. Int. J. Heat Mass Tran. 49, 307–316. https://doi.org/10.1016/j.ijheatmasstransfer.2005.06.022

Di Niso, F., Gaudiuso, C., Sibillano, T., Paolo, F., Ancona, A., Lugarà, P.M., 2014. Role of heat accumulation on the incubation effect in multi-shot laser ablation of stainless steel at high repetition rates. Opt. Express 22, 12200–12210. https://doi.org/10.1364/OE.22.012200

Dumitru, G., Romano, V., Weber, H.P., Sentis, M., Marine, W., 2002. Femtosecond ablation of ultrahard materials. Appl. Phys. A-Mater. 74, 729–739. https://doi.org/10.1007/s003390101183

Eaton, S.M., Zhang, H., Ng, M.L., Li, J., Chen, W.-J., Ho, S., Herman, P.R., 2008. Transition from thermal diffusion to heat accumulation in high repetition rate femtosecond laser writing of buried optical waveguides. Opt. Express 16, 9443–9458. https://doi.org/10.1364/OE.16.009443

Eberle, G., Wegener, K., 2014. Ablation study of WC and PCD composites using 10 picosecond and 1 nanosecond pulse durations at green and infrared wavelengths. Physcs. Proc. 56, 951–962. https://doi.org/10.1016/j.phpro.2014.08.115

Echlin, M.P., Straw, M., Randolph, S., Filevich, J., Pollock, T.M., 2015. The TriBeam system: Femtosecond laser ablation in situ SEM. Mater. Charact. 100, 1–12. https://doi.org/10.1016/j.matchar.2014.10.023

Farsari, M., Filippidis, G., Zoppel, S., Reider, G. A., Fotakis, C. 2007. Micromachining of silicon carbide using femtosecond lasers. J. Phys. Conf. Ser. 59, 84–87. https://doi.org/10.1088/1742-6596/59/1/018

Fujimoto, J.G., Liu, J.M., Ippen, E.P., Bloembergen, N., 1984. Femtosecond Laser Interaction with Metallic Tungsten and Nonequilibirium Electron and Lattice Temperatures. Phys. Rev. Lett. 53, 1837–1840.

Garay, J.E., 2010. Current-Activated, Pressure-Assisted Densification of Materials. Annu. Rev. Mater. Res. 40, 445–468. https://doi.org/10.1146/annurev-matsci-070909-104433

Häfner, T., Heberle, J., Dobler, M., Schmidt, M., 2016. Influences on incubation in ps laser micromachining of steel alloys. J. Laser Appl. 28, 022605. https://doi.org/10.2351/1.4944445

Jahan, M.P., Rahman, M., Wong, Y.S., 2011. A review on the conventional and micro-electrodischarge machining of tungsten carbide. Int. J. Mach. Tool. Manu. 51, 837–858. https://doi.org/10.1016/j.ijmachtools.2011.08.016

Kim, H.C., Yoon, J.K., Doh, J.M., Ko, I.Y., Shon, I.J., 2006. Rapid sintering process and mechanical properties of binderless ultra fine tungsten carbide. Mat. Sci. Eng. A-Struct. 435–436, 717–724. https://doi.org/10.1016/j.msea.2006.07.127

Liu, X., Du, D., Mourou, G., 1997. Laser ablation and micromachining with ultrashort laser pulses. IEEE J. Quantum Elect. 33, 1706–1716. https://doi.org/10.1109/3.631270

Martínez-Torres, P., Mandelis, A., Alvarado-Gil, J.J., 2009. Photothermal determination of thermal diffusivity and polymerization depth profiles of polymerized dental resins. J. Appl. Phys. 106, 114906. https://doi.org/10.1063/1.3266007

Neuenschwander, B., Jaeggi, B., Schmid, M., Dommann, A., Neels, A., Bandi, T., Hennig, G., 2013. Factors controlling the incubation in the application of ps laser pulses on copper and iron surfaces. In: Xu, X., Hennig, G., Nakata, Y., Roth, S.W. (Eds.), Laser Applications in Microelectronic and Optoelectronic Manufacturing XVIII, Proc. of SPIE vol. 8607, Bellingham, WA, United States, pp. 1-10. https://doi.org/10.1117/12.2004136

Nolte, S., Momma, C., Jacobs, H., Tünnermann, A., Chichkov, B.N., Wellegehausen, B., Welling, H., 1997. Ablation of metals by ultrashort laser pulses. J. Opt. Soc. Am. B 14, 2716–2722.

Oosterbeek, R.N., Corazza, C., Ashforth, S., 2016. Effects of dopant type and concentration on the femtosecond laser ablation threshold and incubation behaviour of silicon. Appl. Phys. A-Mater. 122, 449. https://doi.org/10.1007/s00339-016-9969-y

Page, K., Li, J., Savinelli, R., Szumila, H.N., Zhang, J., Stalick, J.K., Proffen, T., Scott, S.L., Seshadri, R., 2008. Reciprocal-space and real-space neutron investigation of nanostructured Mo2C and WC. Solid State Sci. 10, 1499–1510. https://doi.org/10.1016/j.solidstatesciences.2008.03.018

Perecherla, A., Williams, W.S., 1988. Room-Temperature Thermal Conductivity of Cemented Transition-Metal Carbides. J. Am. Ceram. Soc. 71, 1130–33.

Pfeiffer, M., Engel, A., Weißmantel, S., Scholze, S., Reisse, G., 2011. Microstructuring of steel and hard

metal using femtosecond laser pulses, Physcs. Proc. pp. 60–66. https://doi.org/10.1016/j.phpro.2011.03.106

Pham, K.X., Tanabe, R., Ito, Y., 2013. Laser-induced periodic surface structures formed on the sidewalls of microholes trepanned by a femtosecond laser. Appl. Phys. A-Mater. 112, 485–493. https://doi.org/10.1007/s00339-012-7437-x

Ready, J.F., 1971. Effects of High-Power Laser Radiation. Academic Press, Inc., New York.

Rethfeld, B., Sokolowski-Tinten, K., von der Linde, D., Anisimov, S.I., 2004. Timescales in the response of materials to femtosecond laser excitation. Appl. Phys. A-Mater. 79, 767–769. https://doi.org/10.1007/s00339-004-2805-9

Sugioka, K., Cheng, Y., 2014. Femtosecond laser three-dimensional micro- and nanofabrication. Appl. Phys. Rev. 1, 041303. https://doi.org/10.1063/1.4904320

Upadhyaya, G.S., 2001. Materials science of cemented carbides—an overview. Mater. Design 22, 483–489.

von der Linde, D., Sokolowski-Tinten, K., Bialkowski, J., 1997. Laser–solid interaction in the femtosecond time regime. Appl. Surf. Sci. 109–110, 1–10. https://doi.org/10.1016/S0169-4332(96)00611-3

Wang, H., Webb, T., Bitler, J.W., 2015. Study of thermal expansion and thermal conductivity of cemented WC-Co composite. Int. J. Refract. Met. H. 49, 170–177. https://doi.org/10.1016/j.ijrmhm.2014.06.009

Weber, R., Graf, T., Berger, P., Onuseit, V., Wiedenmann, M., Freitag, C., Feuer, A., 2014. Heat accumulation during pulsed laser materials processing. Opt. Express 22, 11312–11324. https://doi.org/10.1364/OE.22.011312

Chapter 2

High energy ball milled stainless steel 17-4PH and cobalt chromium for additive manufacturing alloy design

Kendrick Mensink,[a,b] Christian Roach,[a,c] Mádelyn Madrigal Camacho,[a,d] Guillermo Aguilar,[a,e] and Suveen Mathaudhu,[a,f]

[a]*Department of Mechanical Engineering, University of California, Riverside, CA, 92521, USA*

[b] *kmensink@engr.ucr.edu*

[c] *croach@engr.ucr.edu*

[d] *madelyn.madrigalcamacho@email.ucr.edu*

[e] *gaguilar@engr.ucr.edu*

[f] *smathaudhu@engr.ucr.edu, corresponding author*

Abstract: Metallic additive manufacturing (MAM) has been limited to a subset of alloys that lend themselves well to the rapid heating, rapid cooling cyclic thermal processing applied by laser or electron beam. Ti6Al4V, Inconel 718, stainless steel 316L and 17-4PH are some of the most common commercial alloys and accordingly have been researched heavily for optimal processing and properties in a variety of ways. Obstacles that have limited the exploration of new alloys that are amenable to the MAM process include poor understanding of defect formation in relation to thermal parameters, cost of synthesizing new alloys, and low throughput studies of the feasibility of newly developed alloys. To address some of these limitations and explore the possibility of MAM alloy design with non-spherical, high surface roughness milled particles, we compare the Hall

flow and K40 CO_2 laser-sintered density, microstructure and phase formation of two systems: 1) commercially atomized 17-4PH vs atomized then high energy ball milled stainless steel 17-4PH and 2) commercially atomized CoCr vs elemental Co and Cr powders alloyed by high energy ball milling. This approach helps qualify high energy ball milling and low powered laser coalescence as a platform for alloy design and testing for MAM.

Introduction

2.1.1 MAM limitations

Metal additive manufacturing (MAM) can produce parts with almost any geometry and design, with minimal waste, lending itself well to rapid, relatively inexpensive prototyping. Small-scale manufacturing using MAM Powder Bed Fusion (PBF) has penetrated certain markets such as aerospace and biomechanical components due to complex and individually customized geometry requirements. However, other markets and large scale PBF MAM is limited by common issues like void formation, cracks, anisotropic behavior, and a lack of standards and guidelines for MAM process and quality parameters (Ngo et al., 2018). Key areas projected to be paradigm shifts towards avoiding processing defects and making MAM more useful include a priori “feed forward” model-based process controls (King et al., 2015), in-situ sensor monitoring feedback, and the development of materials tailored specifically to MAM processing. Furthermore, platforms to relatively quickly and easily synthesize and test new materials for MAM is lacking.

The “black box” nature and prohibitive cost of commercially available MAM equipment and maintenance has limited further development of MAM materials and techniques for some researchers, hobbyists, and companies. Therefore, a few have built their own systems to better study process parameters or in-situ monitoring. Cao et al. (2015) built their own custom counter rolling 3D printer to study the feasibility of ultra-thin 55 μm powder layering by double-smoothing mechanism. Bidare et al. (2017) designed and built a portable PBF system for in-situ x-ray imaging to understand heat conduction away from the melt pool and monitor pores across several layers. Those fortunate enough to have access to customizable powder fed (also called directed energy deposition), rather than powder bed, MAM systems have demonstrated remarkable composition control and solidification microstructure analysis.

Others have focused on the relationships between energy source parameters and build quality to optimize processing parameters for specific powders. For example, Gu et al. (2013) studied the influence of one common energy source parameter, energy density, on typical build quality results for Selective Laser Melted 17-4PH stainless steel: porosity and microstructure features. They found energy density alone was not sufficient indicator for porosity, however volume percent martensite was maintained at all tested laser power and scanning speed combinations. Rubenchik et al. (2018) simplified the complex laser-induced temperature distribution and melt pool dimensions to two characteristic dimensionless parameters: the ratio of laser deposited energy density to the melt enthalpy and the ratio of dwell time to thermal diffusion time, for any material. Modeling the

thermal distribution is useful, but it typically does not predict the non-equilibrium solidification related defects that so often determine if a build is acceptable.

2.1.2 Suitable MAM material traits

Even assuming the melt enthalpy, thermal diffusion time and therefore temperature distribution of any potential MAM material can be found, what material systems respond well to the rapid, localized thermal gradient nature of the laser PBF process? Which specific properties need to be optimized? Similar to how Verbelen, (2016) identified properties related to processability and screened materials for polymer laser sintering, an "PBF-ability" of metal systems should include material performance, recyclability, flowability in powder form, coalescence under laser, melt flow, similar molten and solid density, solidification behaviors, and solidification temperature range. Bourell et al. (2017) notes fcc nonferrous metals are more defect tolerant than other metals. They also noted that AM metal systems must be both weldable and castable. They have relatively high viscosity melt pools, do not exhibit deleterious behavior under high heat gradient and have an ability to withstand large thermal and shrinkage-induced residual stress without cracking. Microcracks can be caused by embrittlement in the heat affected zone (HAZ), solidification, or precipitation formation. Macrocracks can be caused by incomplete melting or fusion, as Spierings et al. (2011) found. High liquid surface tension can benefit coalescence at early viscous sintering stages, but also exhibit undesirable balling phenomena at certain processing parameters. Feedstock with entrapped gas leads to residual porosity. To make prediction more difficult, properties of common AM

materials are not typically known at the non-equilibrium states a material is subject to in PBF processing.

Non-equilibrium microstructure often results from the cyclic and rapid local thermal processing. Solidification microstructure type (equiaxed, columnar, cellular, planar) and relative size can be estimated, though not probed, from modeling solidification rate, R, and temperature gradient, G, at melt pool boundary as reported by Lee et al., (2014) for laser deposition processing. Thus far there are only about a dozen common commercial metal PBF materials including pure titanium, Ti6Al4V, 316L stainless steel, 17-4PH stainless steel, maraging steel, AlSi10Mg, CoCrMo, and Inconel nickel-based superalloys. According to Bourell et al.'s review, Ti6Al4V has only a 10 K solidification range and predominately solidifies into vertical columnar bcc β microstructure which transform to hcp α' martensite upon quenching in PBF, and the melt pool boundaries are not obviously visible. Most other materials form cellular-dendritic microstructure upon solidification likely due to unstable solidification from compositional gradient over larger solidification ranges and have visible melt pool boundaries. For MAM, oxide layers are detrimental to uniform sintering for many alloys such as aluminum based, which forms a stable Al_2O_3 surface layer, so carefully controlled sintering atmospheres must be used. In addition, each metal system and particle size distribution (PSD) has unique laser absorption spectrum, so once two of the following three items are chosen, the third can be optimized to maintain an effective melt pool: wavelength, metal system/PSD (absorption), and laser power density/scan speed.

2.1.3 Powder flow

Beyond the material system considerations such as intrinsic melting point, phase formation, affinity for oxygen, etc., the flowability of the powder is important to the "AM-ability" because both PBF and directed energy deposition-type MAM spread 100% of the manufacturing powder. Shape, size, surface roughness, surface composition, interparticle attractive forces (electrostatic, hydrogen), humidity, moisture, temperature, and PSD are factors for flowability of each powder batch. The largest particles in the PSD obviously limits the effective layer height, and the powder surface composition and roughness affect interparticle friction. Jacob et al., (2018) found that particle size and PSD have significant effects on apparent and powder bed densities. Higher powder bed density was achieved with wider PSD and a greater fraction of the PSD in the size range of the layer thickness. Powder bed density affects thermal distribution and post-fusion density. Haeri et al. (2017) found that rollers spread powder with greater powder bed density and lower roughness than blades, but warned that powder with mixed aspect ratios tended to distribute the higher aspect ratio particles higher in the bed layers. Spierings et al. (2016) noted the tendency to use finer powder sizes to improve microstructure, part density, surface quality and scan speed. However, they warned of the potential downsides of finer powder sizes: increased particle-particle bonding and therefore unacceptable flowability, and ejection and reactivity due to higher specific surface area and low mass. Smaller particle sizes and higher aspect ratio powders have poorer flow properties, which Hou and Sun (2008) found using a ring shear tester for low density microcrystalline cellulose. However, flow quantifications should match the stress

state of the application. A modified Elcometer 4340, developed by Verbelen (2016), matches the stress state of PBF processing very well. Spierings et al. (2016) argued for using optical evaluation to quantify AM powder flowability using techniques of avalanche angle, Hausner ratio, volume expansion ratio and surface fractal. However, they noted that Hall flow funnel measurement was more like AM flow conditions than static tests like the Ring shear cell and that a there is a flow benefit of lower loose-pack density: reduced inter-particle forces. There have been powders that do not flow in Hall funnels, yet still produce full density parts in laser AM machines [KU Leuven copper, 3DS 17-4], so while the community seems to agree that powder flowability is important, critical flowability for MAM and a dominant flow test have not been clearly shown. In this work we report on Hall-style funnel tests as a function of particle size.

2.1.4 MAM powder production and testing

Feedstock materials are typically pre-alloyed via gas atomization. The composition and size distribution used in MAM production are carefully controlled. While atomization produces powder that is very spherical and of uniform composition, Anderson et al., (2018) have suggested some approaches to address the inability to control the atomization-yielded PSD. Powder feedstock that is not produced by atomization include powders thermally sprayed, Dietrich et al. (2016), and milled, this work and the next section. It is worth noting that Gu et al. (2012) reviewed compositionally, and therefore functionally, graded MAM from individually controlled elemental powder flow rates, which opens the door for locally tailored microstructure and properties in a single part. Batch-level exploration is well-suited to testing novel MAM materials. However, it has

been done mostly in directed energy deposition. In this work we show it can be done with small-batch simulated PBF.

2.1.5 MAM with milled powders

The approach to develop MAM-tailored materials has been largely trial and error. Several researchers have tried milling powders for MAM-related projects. Fullenwider et al., (2019) have shown an ability to produce mostly spherical ball milled powders by optimizing a two-stage milling process, the first step uses large balls to refine (recycled machining chipped) particle size, and the second step to spheroidize. Besides achieving a PSD fit for "powder-fed" fusion, 38-150 μm, they showed higher particle hardness and successful laser adhered tracks. Gu et al., (2014) showed earlier that planetary mixing of atomized AlSi10Mg powder with TiC nanopowder could be >98% densified with optimized laser energy density. The milling and higher laser energy density processing resulted in dispersed nano TiC reinforcement and superior wear resistance. Other work by Han et al., (2017), (2016); Jue et al., (2017) focused on Al-Al_2O_3 composites, demonstrating their good feasibility for wear applications and MAM-ability by PBF. These works show that small batch ball-milled production of tailored materials, whether recycled or composite-mixed, can have proper flowability and fusibility for MAM.

For this work, we focus on a simpler binary alloy already commonly used and optimized (by Wang et al., 2018) for MAM, cobalt chromium, without explicit reinforcement phase mixed in. This alloy is commonly used in implants and wear applications due to its wear and corrosion resistance, and high specific strength. The Cr-rich sigma (σ) phase was found to benefit wear properties of a solid solution HCP (ε) matrix alloy when it

precipitated during high energy ball milling and spark plasma sintering densification. It was not clear whether the milling or densification process was primarily responsible for the σ or ε formation. Therefore, we perform similar milling steps as Wang et al., and explore the phase formation before and after laser coalescence.

2.1.5 Rationale for the inexpensive, high-throughput particle shape comparison study

The promise of rapid, customizable and inexpensive prototyping and production has driven the recent research and development of AM materials. As an initial step towards developing metal systems that are better tailored to the PBF process, we use an inexpensive, highly controllable, monitored laser system to study the feasibility of using milled powder for alloy development purposes. We compare milled powder to traditional atomized powder for flowability and sinterability, noting differences in initial morphology and PSD, for stainless steel 17-4PH and CoCr, common MAM alloys. This approach forecasts feasibility for high-throughout, bottom-up, small-batch MAM alloy development using mainly a SPEX mill and K40 laser cutter. However, inferior initial powder packing and final density when using milled powders in multi-layer MAM has yet to be studied and could nullify the potential benefits of milled powder production explored in this work.

Methods and Materials

2.2.1 Powder production

Milling and atomization offer two very different approaches to creating a powder batch which are described in detail elsewhere. See Fig. 5 for a visual reference of their working

mechanisms. Gas and water atomized powders currently monopolize the MAM feedstock market. Their relative strengths and weaknesses for MAM are shown in Table 2.

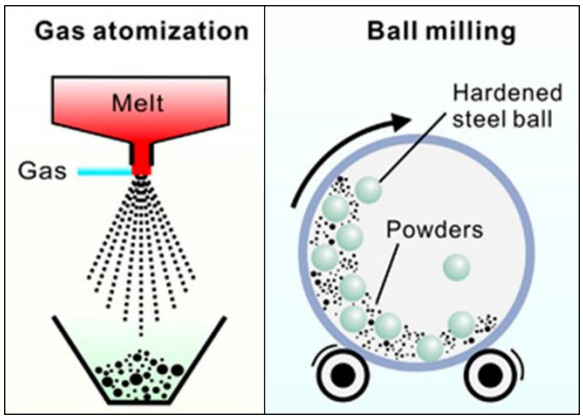

Figure 5. Comparison of atomization and milling powder production processes

Experiments compared commercially available atomized to high energy ball milled (SPEX) powders, see Table 2. A batch of commercially available stainless steel 17-4PH powder with average size of 4 μm and size range of 0 to 20 μm was chosen for comparison because it was known to produce near full density prints using a 3D Systems ProX DMP 200. Ten grams from the same batch of stainless steel 17-4PH powder was further processed by milling to see the effects of contamination, size distribution, morphology and surface roughness on Hall flowability and laser sinterability for the same nominal composition. After milling for 20 hours in a SPEX 8000D mill, the particle size distribution is shown in Fig. 7b. The milling time required to mechanically alloy metal systems if often less than 20 hours, so this amount of time was chosen for the 17-4 powder to help validate results for future mechanically alloyed powders. Between five and seven grams of powder were milled in each jar. The ball to mass ratio was 5:1, and 1 wt% stearic acid was used as a process control agent to help lubricate the powder and prevent agglomeration. To avoid heat buildup, the mill ran cycles of 2 minutes on, 1

minute off. The jars were sealed and opened in an argon filled glovebox to limit oxygen exposure. After milling, powders were ground with agate mortar and pestle for 15 minutes, and then sieved with 230 (63 μm opening), 325 (45 μm), 430 (32 μm), and 635 (20 μm) meshes (Gilson Co).

Table 2. Characteristics of ball milled and atomized powders for metal additive manufacturing

	Ball milled powder	Atomized powder[a]
Porosity	**No internal porosity due to compressive action**	Occasional internal trapped gas porosity that remains in as-built parts
Surface roughness	Very high	Low, smooth due to droplet solidification in vacuum
Particle shape	Irregular, non-spherical, without satellites	Spherical with occasional satellites
Size distribution	Varies with milling parameters 0-200 μm in this work	Varies with nozzle type and flow conditions Typically 0-500 μm, low yield in range for MAM: 20-150 μm
Throughput	Varies with mill size 10-15 g per SPEX mill batch in this work **Can be made of any alloy/composition**	Varies with mill size Typically very high (kg batches) Requires exact composition ingot
Grain size	Typically ultra fine due to severe plastic deformation refinement	Varies with droplet size Typically fine due to solidification rate
Flowability	Hall flow rates found to be ~60% of atomized in this work	Typically highly flowable
Purity	Typically low, contaminated by process control agents, milling balls and jar **Allows some control of meta-stable phases**	Typically very high, water removal required for water atomization

Table 2 [a](Anderson et. al., 2018)

To demonstrate the ability to design and test new MAM material compositions using a milling process, elemental powders (Co, 99.9%; Cr, 99.8%, Micron Metals) were mechanically alloyed for 12 hours in proportion to match the composition of commercially available atomized cobalt chromium, see Table 3. Zhao et al., (2019) found

that 12-hour SPEX milled CoCr powders produced exceptionally high hardness and wear resistance after consolidation by SPS. This improved performance was credited to the common CoCr gamma (FCC) phase exclusion, which was transformed by milling to ultrafine-grained epsilon (HCP) phase with nano sigma (Tetragonal) phase precipitates. This work explores if similar microstructure performance benefits occur with laser consolidation.

2.2.2 Powder characterization

The size distributions for the two stainless and two CoCr powders after atomization and/or milling is shown in Fig. 7. Visual light microscopy (Nikon Eclipse LV 100D-U) was used to capture images of the various particles, dispersed in ethanol. ImageJ software was used to threshold and measure individual particle areas, which were assumed to be spherical for the purpose of reported PSD in terms of particle diameter.

Scanning electron microscopy (FEI NNS450) was used to capture images of particle shape and morphology (Fig. 7, 10c, 10d). Transmission electron microscopy (FEI Technai T12) was used to capture images and selected area electron diffraction patterns of some of the smallest electron transparent atomized and milled CoCr powders (Fig. 11).

X-ray diffraction (PANalytical Empyrean Series 2) was used for phase identification to estimate phase fraction of the atomized and milled powders (Fig. 10a, 10b).

Hall flow (ASTM B213) was used to compare powder flowability. Flow tests were done for different sieved particle size ranges, mixtures of size ranges using only seven grams (Fig. 8a) and for the standard fifty grams (Fig. 8b). A Hall funnel was machined from

aluminum and the powder-contacting surface was polished. A video (60 frames per second) recording of the powder exiting the funnel was used to measure flow rates. Thermal gravimetric analysis and differential scanning calorimetry (Mettler Toledo TGA/DSC 3+) was done to compare the atomized and milled CoCr powder kinetics (Fig. 12).

Table 3. Powder production routes used

System	Atomization process (first)	Milling process* (second)	Referenced as	Significance
Stainless steel 17-4PH	Commercial (3D Systems)	None	S-atomized	Industry standard
Stainless steel 17-4PH	Commercial (3D Systems)	20 hours	S-atomized/milled	Milled version of industry standard
Cobalt-22.6 wt% chromium	Commercial (ATI)	None	C-atomized	Industry standard
Cobalt-22.6 wt% chromium	None	12 hours	C-milled	Mechanically alloyed from separate cobalt and chromium elemental powders

Table 3 *SPEX 8000D; 5:1 ball to power mass ratio; 2 minute on, 1 minute off cycles; 1 wt% process control agent (stearic acid), at room temperature, 1/8" stainless steel 440C balls, stainless steel 440C jars

2.2.3 Laser processing

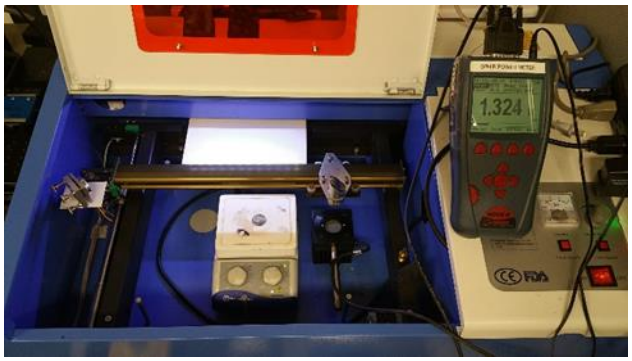

Figure 6. Laser processing equipment (K40 CO_2 laser cutter, Linkam heated stage, Ophir Nova II 50 W power head, copper/graphite cups, argon cover gas)

Immediately prior to laser irradiation tests, powders were held at over 100°C (heated stage) with argon cover gas for at least ten minutes to minimize moisture, see Fig. 6. An inexpensive CO_2 laser source (K40) was positioned (via K40 laser cutting software) over a small cup. The cup had threefold purpose: 1) hold just enough powder to simulate a powder bed fusion process (~five mm diameter, ~600 um deep); 2) be able to withstand the focused CO_2 laser energy without bonding to the adjacent melted powders (copper, graphite and alumina exhibited these qualities); and 3) conduct (in the case of copper) or insulate (graphite, alumina) thermal energy absorbed by the metal powders as well as conduct heat from the heated stage for preheating of powders. The powder surface was positioned near the minimum beam waist [about 100 μm] five centimeters from the focal lens. Laser power was measured using an Ophir Nova II and 50 W power head and set to the highest stable power (12 W) immediately before each laser sintering experiment. Hatch spacing, scan speed, and raster pattern (scan strategy) were controlled by open source stage controller software (K40 Whisperer). The heated stage with raised to 600 °C immediately before each experiment to reduce thermal stress-induced cracks, however the preheated temperature of the powder surface was typically between 150 and 400 °C.

2.2.4 Coalesced layer characterization

After the laser raster process finished, the coalesced powder is allowed to cool inside the cup with assistance of the flowing argon cover gas to near room temperature. The sintered or melted top layer is removed from the cup and is strong enough to handle for imaging, thickness, and density analyses.

Archimedes method, with propylene glycol as surrounding fluid, is used to measure density. Propylene glycol has the advantages of being colorless, clear, hygroscopic, and better than water in terms of slower evaporation rate, less reactive with metals, and higher surface tension and therefore less penetration into pores. The average of at least three buoyancy measurements is reported in Fig. 9.

X-ray diffraction was used again for phase identification and to estimate crystallite size and phase fraction after laser processing (Fig. 10b).

Berkovich nano hardness (Nanovea Mechanical tester) was measured at polished laser coalesced cross sections (not reported in this work).

Electron microscopes (FEI NNS450 SEM with EDS, FEI Technai T12 TEM) were used to characterize the laser-coalesced powder layer microstructure (Fig. 7, 10, 11).

Results and Discussion

2.3.1 Powder size

Each type of MAM has optimal particle size distribution. Typically, laser powder bed fusion is 15-45 μm, electron beam powder bed fusion is 45-106 μm, and powder fed is 45 to 75 μm (Anderson et al., 2018). A powder production method that could precisely control the output size to match these ranges would be ideal, but unfortunately both atomization and milling production techniques generally produce particle size distributions larger than those desired for MAM, which increases the cost and decreases the availability of desired powders.

Size distribution is important for powder packing “apparent” density (ASTM D7481), especially in the powder bed. Fine particles can occupy the space between larger

particles. Wide size distribution, with more fine sizes, improves conventional sintering density and in at least one case, (Liu et al., 2011), also selective laser melting density. However, high apparent density reduces flowability. Higher packing density has been correlated with higher powder bed density (Jacob et al., 2018), which has also been shown to result in higher sintered final density (Zhu et al., 2007).

Size also affects the flowability. Very fine particles have high surface to volume ratio and are strongly affected by interparticle friction, van der Waals forces and agglomeration, and so tend to have less flowability.

The commercial atomized powders were already sieved by the manufacturer, <20 μm 17-4PH and <45 μm CoCr. The 20-hour SPEX milling process produced larger average size and much broader size distribution for the already atomized and finely sieved 17-4. The large particle size was due to process control agent burn off during such a long 20-hour milling time. The 12-hour SPEX milling of fine Co (0.7-1 μm) and larger Cr (<150 μm) resulted in much finer mechanically alloyed CoCr particles.

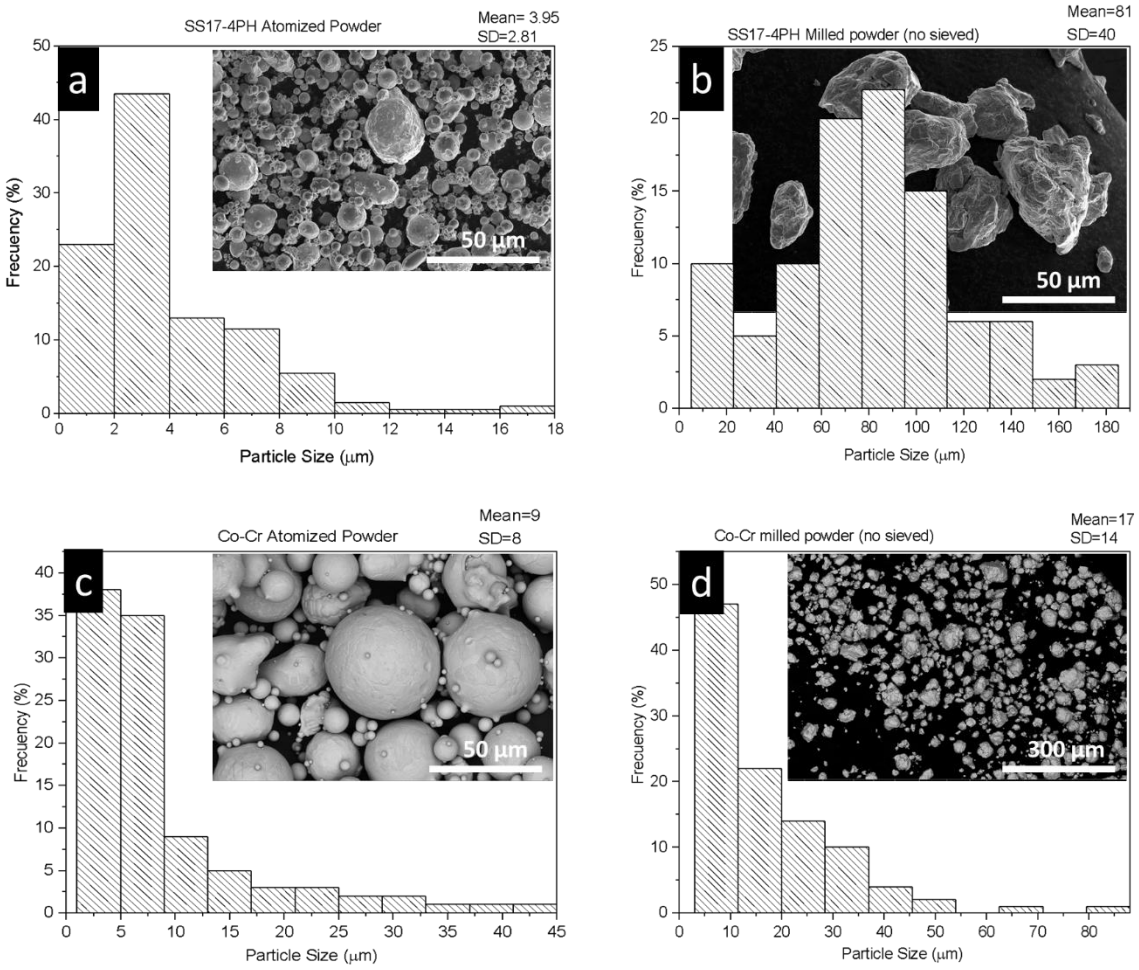

Figure 7. Comparative particle size distributions and SEM images of a) S-atomized, b) S-atomized/milled, c) C-atomized, d) C-milled. See Table 3 for processing details.

2.3.2 Particle morphology

As seen in Fig. 7, atomized particles have smoother surfaces and are more spherical, while the high energy ball milled particles are more irregularly shaped with rough surfaces. Spherical powders will flow under the influence of gravity more easily than non-spherical, and smooth particle surfaces are preferred to rough surfaces or surfaces with attached satellites (Sames et al., 2016). Fine satellite particles are evident in both S and C-atomized particles, which is known to reduce apparent density and flowability.

2.3.3 Powder flowability

For small batch sizes and high throughput flow testing, the Hall flow funnel is relatively quick and easy to perform. A Hall flow funnel lathed out of aluminum (30° funnel, 0.1-inch diameter orifice, 0.125-inch orifice length) was used to determine whether a powder flowed, driven only by gravity and occasionally an encouraging tap. If the powder flowed, the flow rate was calculated as by dividing a weighed powder mass by the video-recorded time for the funnel to empty. The standard deviation of five tests are the vertical error bars in Fig. 8a. To avoid moisture, Hall flow tests were done in an argon-filled glovebox. The ASTM B213 standard requires 50 grams per test, however only about 10 grams were harvested per milling batch, so the tests were modified using only seven grams for various milled powders.

Figure 8a shows (in blue) the narrow S-atomized/milled particle size range that exhibits the highest flow rate is 32-45 μm. The red crosshairs show flow rates for equal mixtures of the two corresponding size ranges. Lumay et al., (2012) noted that particles below about 50 μm can have flow behavior dominated by cohesion between particles, while particle shape has little influence. Particles above 50 μm begin to have flow also affected by shape. The mass flow rate of seven grams is about 25% higher than for 50 grams, from Fig. 8b. Flow rates comparison between atomized and milled powder has not received much research attention. It is generally accepted and expected that atomized powder morphology is correlated with superior flowability when compared to milled powder morphology in dynamic flow tests, and that is shown by the lower flow rate of C-milled in Fig. 8b (gray).

We observed the milled powder consistently flowed through the funnel, while some batches of the S-atomized powder stuck and would not flow even with vigorous encouragement. It is likely that residual moisture increased particle cohesion and inhibited the flowability of these atomized powders, considering they were stored in air and for much longer than the recently milled powers. In light of this observation and recent work that used a milling approach to recycle machine chips for MAM (Fullenwider et al., 2019), we predict that milling processes should be useful to "refresh" particles whose surfaces are severely oxidized or moisture-adsorbed, thereby increasing the usefulness of previously considered unusable contaminated powders.

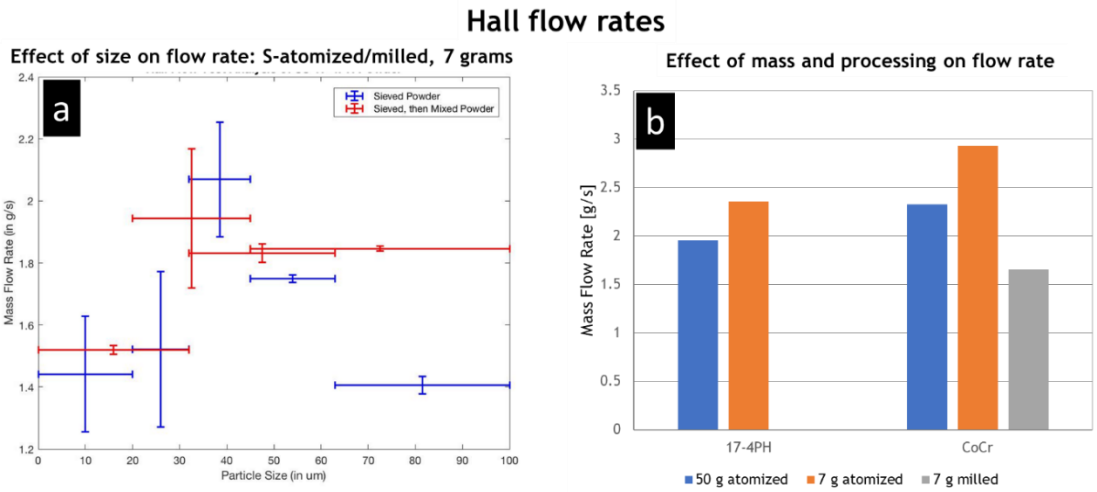

Figure 8. Comparisons of Hall flow (after ASTM B213) rates for a) narrower size ranges (blue), and broader size ranges (red); and for b) 50 vs 7 grams of S-atomized, C-atomized, and C-milled.

It is important to note that Hall flowability does not directly indicate if a powder is processable with MAM. The S-atomized powder in this work was able to produce fully dense parts in a ProX 200 DMP, but often failed to flow in Hall flow funnel and might fail in other MAM machines.

2.3.4 Coalesced powder characterization

To date, the high cost of high power laser sources, much less MAM OEM equipment and feedstock has repressed more widespread research in laser MAM. Using a low cost ($400) laser that would commonly be assumed too low in power density to affect metals at all, we demonstrate that preliminary laser sintering studies can be achieved if using only a few grams of fine powders thanks to their increased absorption (Trapp et al., 2017).

Wang et al., (2018) studied the optimal laser speed and power with 50 μm hatch for CoCr selective laser melting and found 160 W (1071 nm laser) and 1100 mm/s were near ideal (power/speed = 0.145). Although 1071 and 10,600 nm wavelength have different absorption, and research has shown maintaining the power to speed ratio for different powers and/or speeds yields different thermal conditions and resultant solidification microstructure and properties, the same hatch and ratio of power to speed was used for simplicity with the K40 CO_2 laser. It so happened that this power/speed proved somewhat optimal and yielded smoother and more densely coalesced powder layers than neighboring powers/speeds/hatches, although the K40 laser parameter space was not fully explored. The highest stable power of our particular K40 laser (12 W) was used in all experiments. A scan speed of 82.5 mm/s gives the 0.145 power/speed ratio. Fluence rates of 0.6-7 MW/m^2 (an order of magnitude below typical selective laser melting powers) were able to melt each type of powder listed in Table 3.

The actual energy absorbed by the powders resulting in heating and sintering or melting varies by several items, most of which are difficult to match between different laser

MAM machines. These include oxide layer formation (feedstock history and gas environment), apparent density, laser power (Haag et al., 1996), heat transfer conditions (build plate and gas flow convection), particle shape and size (Boley et al., 2015), material type, laser intensity and wavelength, and whether the powder has melted (Trapp et al., 2017).

The copper cup conducted the heat away from the laser-heated powder faster than a powder bed would, yet due to copper's high reflectivity to CO_2 wavelength (10.6 μm), the copper cup did not heat nor bond with powder, so heat was likely not conducted away as fast as in the case of PBF melting of one un-melted layer of powder with a solid part beneath.

Figure 9. Comparison of atomized and milled particle laser coalesced layer thickness and Archimedes densities. All cases were coalesced with 12W, 82.5 mm/s, and 50 μm hatch.

The sintered density using a K40 laser source is likely hindered not only by low power-induced melt pool instability, but also by its comparatively large spot size. (Liu et al., 2011) noticed lower densities when using larger laser spot sizes between 26 and 48 μm on atomized stainless 316L powders.

The XRD plot in Fig. 10b shows the atomized powder maintains dual FCC/HCP phases after laser processing. The EDS element maps in Fig. 10c, 10d show that the Co and Cr are well dispersed in individual atomized particles. The particle shown was cut in half by focused ion beam to reveal the cross section.

The TEM images shown in Fig. 11 show the crystallite sizes are on the order of 400 nm for C-atomized, but on the order of 50 nm for C-milled. We hypothesize that nanoprecipitation from milling contamination carbides, nitrides, oxides and/or severe plastic deformation-induced sigma Cr-rich tetragonal phase will remain or nucleate during laser melting and help to increase planar boundaries of the sintered parts, which should result in increased hardness and reduced ductility. Further TEM of FIB-cut lamella cross sections is needed to test this hypothesis.

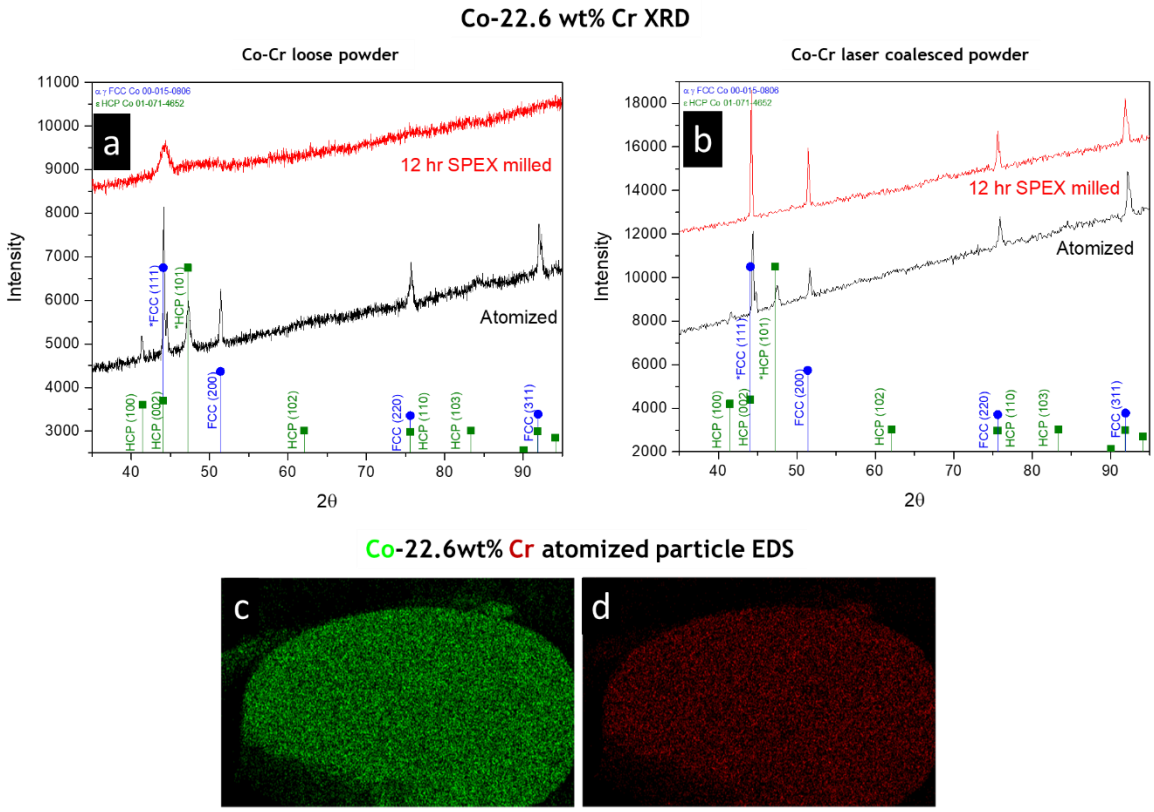

Figure 10. Powder phase identification by (top) x-ray diffraction of C-milled (red) and C-atomized (black) and (bottom) energy dispersive spectroscopy (EDS) element map of Co (green) and Cr (red) of C-atomized particle cut in half by focused ion beam showing no obvious elemental segregation.

Due to the different processing shown in Fig. 5, the atomized particles have much larger crystal size, which can be seen from the two darkfield TEM particles in Fig. 11. Atomized grain sizes appear to be on the order of several hundred nanometers while the milled grains are less than one hundred in the particles shown in Fig. 11. The selected area electron diffraction (SAED) of the milled particle matches the diffraction of HCP Co (green), FCC Co (blue), Co oxides (yellow), Cr oxides (gray), and faintly, tetragonal sigma phase. The presence of small amounts of sigma phase after milling may correlate to sigma found by Zhao et al., (2019).

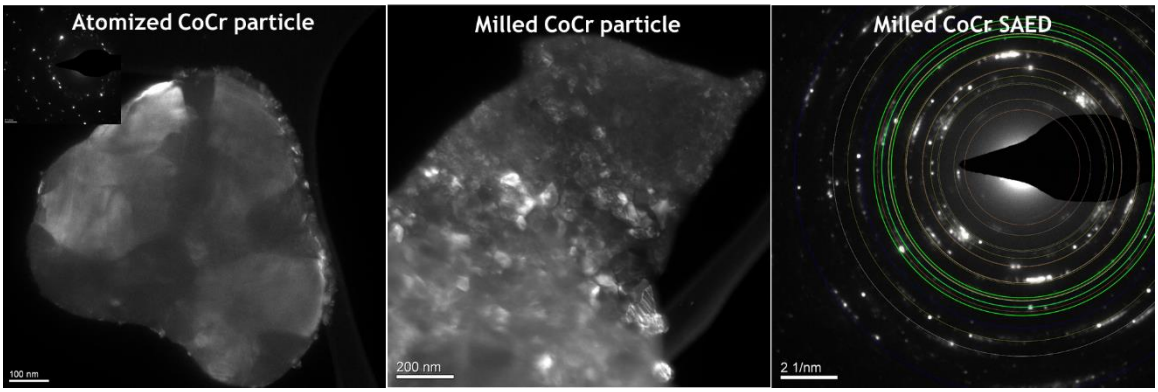

Figure 11. Transmission electron microscopy images of drop cast atomized and milled particles before laser coalescence, grain size difference is evident. The selected area electron diffraction (SAED) of the milled particle is shown with overlaid diffraction rings for FCC, HCP, and tetragonal phases or Co, Cr, and oxide phases.

Fig. 12 shows initial drops in mass change (blue lines) up to about 400 °C, which could be associated with stearic acid burn off for the milled CoCr powder. The atomized powder also loses mass up to 700 °C, but less than the milled. After losing mass, both powders gain mass, possibly from oxide layer forming from impurity in the argon gas flow. The relative mass gains are different, we suspect due to the greater surface roughness and oxide growth potential of milled particles. The sharp dips in the atomized powder between 900 and melt may be due to particles shifting while sintering and small satellites sintering into larger particles. At the much more rapid heating during laser MAM, we suspect the relative mass changes will be less pronounced.

For the heatflow (black lines), there is a dip in the atomized powder at 900 °C, which we hypothesize corresponds to the HCP to FCC transition at the overlaid composition line. From Fig. 10 the atomized powder is dual phase FCC/HCP, and the milled powder appears to be mostly FCC, so the difference in heatflow above 900 °C may in part be due

to atomized HCP to FCC transformation, which would have less time to occur during more rapid laser MAM.

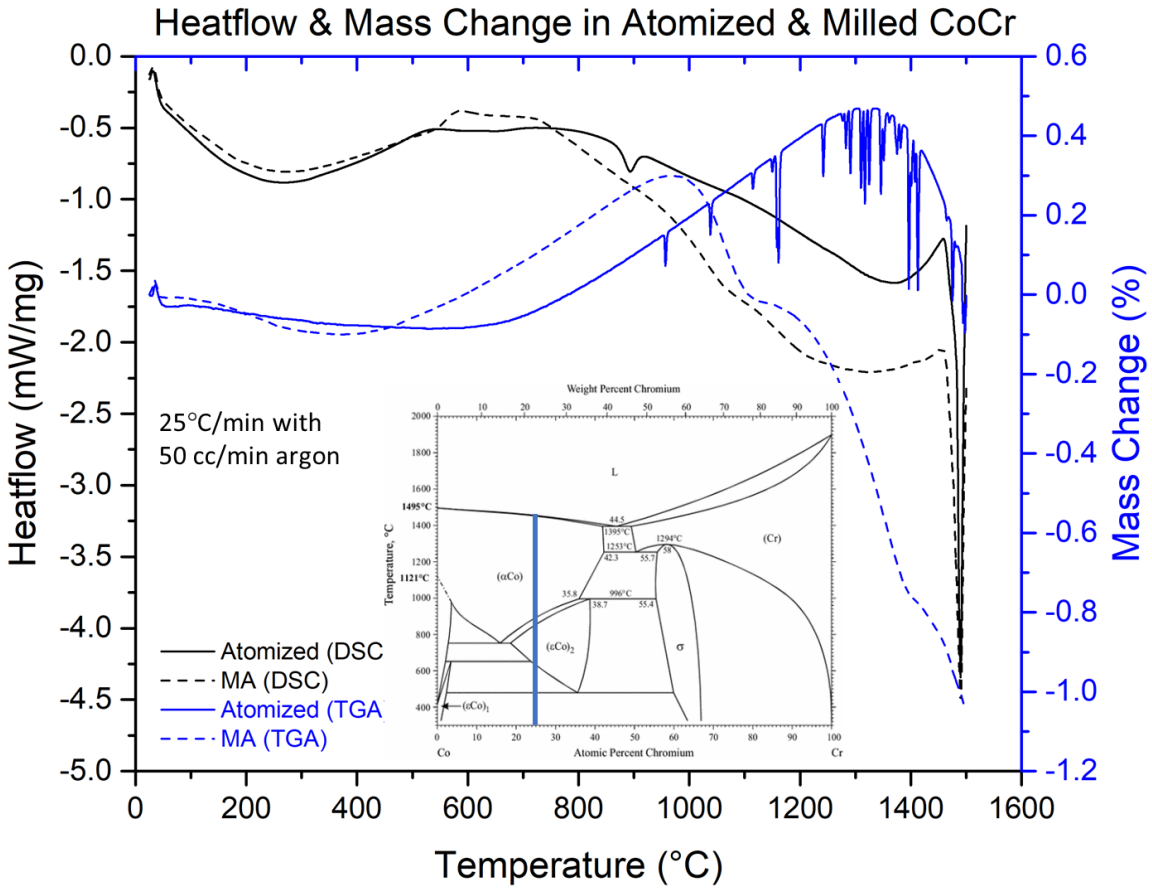

Figure 12. Thermogravimetric analysis and differential scanning calorimetry measurements compared for atomized and milled CoCr loose powders. Inset of the Co-Cr phase diagram showing the equilibrium phase transition from HCP to FCC occurs near 900 °C.

Conclusions

We demonstrated an inexpensive MAM alloy development approach that addresses the ability to synthesize and laser coalesce novel milled materials for scaled up use in laser powder bed fusion, electron beam powder bed fusion, and directed energy deposition.

Despite less than 99% of theoretical density measured for K40 laser coalesced powders, the mechanically alloyed CoCr powder should perform well in OEM AM because 1) stainless 17-4 powders perform well in OEM AM and achieve <95% density with K40 laser, and 2) they will have no internal porosity, and 3) they exhibit consistent dynamic flowability, albeit at about 60% of the atomized counterpart Hall flow rate.

SPEX milling does not produce particle size distribution that match MAM technique ranges, although optimizing the milling time to achieve fully solutionized alloys without PCA burn off and agglomeration can produce very MAM-usable fine particles, provided they are kept clear of cohesive surface effects like moisture in air.

Ball milled powders may fit a niche MAM market for wear and fatigue resistant application due to their lack of internal pores and associated fatigue failure locations.

References

Anderson, I.E., White, E.M.H., Dehoff, R., 2018. Feedstock powder processing research needs for additive manufacturing development. Curr. Opin. Solid State Mater. Sci. 22, 8–15. https://doi.org/10.1016/j.cossms.2018.01.002

Bidare, P., Maier, R.R.J., Beck, R.J., Shephard, J.D., Moore, A.J., 2017. An open-architecture metal powder bed fusion system for in-situ process measurements. Addit. Manuf. 16, 177–185. https://doi.org/10.1016/j.addma.2017.06.007

Boley, C.D., Khairallah, S.A., Rubenchik, A.M., 2015. Calculation of laser absorption by metal powders in additive manufacturing. Appl. Opt. 54, 507–517. https://doi.org/10.1201/9781315119106

Bourell, D., Kruth, J.P., Leu, M., Levy, G., Rosen, D., Beese, A.M., Clare, A., 2017. Materials for additive manufacturing. CIRP Ann. - Manuf. Technol. 66, 659–681. https://doi.org/10.1016/j.cirp.2017.05.009

Cao, S., Qiu, Y., Wei, X.-F., Zhang, H.-H., 2015. Experimental and theoretical investigation on ultra-thin powder layering in three dimensional printing (3DP) by a novel double-smoothing mechanism. J. Mater. Process. Tech. 220, 231–242. https://doi.org/10.1016/j.jmatprotec.2015.01.016

Dietrich, S., Wunderer, M., Huissel, A., Zaeh, M.F., 2016. A New Approach for a Flexible Powder Production for Additive Manufacturing. Procedia Manuf. 6, 88–95. https://doi.org/10.1016/j.promfg.2016.11.012

Fullenwider, B., Kiani, P., Schoenung, J.M., Ma, K., 2019. Two-stage ball milling of recycled machining chips to create an alternative feedstock powder for metal additive manufacturing. Powder Technol. 342, 562–571. https://doi.org/10.1016/j.powtec.2018.10.023

Gu, D., Wang, H., Chang, F., Dai, D., Yuan, P., 2014. Selective laser melting additive manufacturing of TiC / AlSi10Mg bulk-form nanocomposites with tailored microstructures and properties 56, 108–116. https://doi.org/10.1016/j.phpro.2014.08.153

Gu, D.D., Meiners, W., Wissenbach, K., Poprawe, R., 2012. Laser additive manufacturing of metallic components: materials, processes and mechanisms. Int. Mater. Rev. 57, 133–164. https://doi.org/10.1179/1743280411Y.0000000014

Gu, H., Gong, H., Pal, D., Rafi, K., Starr, T., Stucker, B., 2013. Influences of Energy Density on Porosity and Microstructure of Selective Laser Melted 17- 4PH Stainless Steel. Solid Free. Fabr. Proc. 37, 474–489. https://doi.org/10.1007/s13398-014-0173-7.2

Haag, M., Hügel, H., Albright, C.E., Ramasamy, S., 1996. CO2laser light absorption characteristics of metal powders. J. Appl. Phys. 79, 3835–3841. https://doi.org/10.1063/1.361811

Haeri, S., Wang, Y., Ghita, O., Sun, J., 2017. Discrete element simulation and experimental study of powder spreading process in additive manufacturing. Powder Technol. 306, 45–54. https://doi.org/10.1016/j.powtec.2016.11.002

Han, Q., Setchi, R., Evans, S.L., 2016. Synthesis and characterisation of advanced ball-milled Al-Al 2 O 3 nanocomposites for selective laser melting. Powder Technol. 297, 183–192. https://doi.org/10.1016/j.powtec.2016.04.015

Hou, H., Sun, C.C., 2008. Quantifying Effects of Particulate Properties on Powder Flow Properties Using a Ring Shear Tester. J. Pharm. Sci. 97, 4030–4039. https://doi.org/10.1002/jps.21288

Jacob, G., Brown, C.U., Donmez, A., 2018. The Influence of Spreading Metal Powders with Different Particle Size Distributions on the Powder Bed Density in Laser-Based Powder Bed Fusion Processes. NIST Adv. Manuf. Ser. 100–17. https://doi.org/10.6028/NIST.AMS.100-17

Jue, J., Gu, D., Chang, K., Dai, D., 2017. Microstructure evolution and mechanical properties of Al-Al 2 O 3 composites fabricated by selective laser melting. Powder Technol. 310, 80–91. https://doi.org/10.1016/j.powtec.2016.12.079

King, W.E., Anderson, A.T., Ferencz, R.M., Hodge, N.E., Kamath, C., Khairallah, S.A., Rubenchik, A.M., 2015. Laser powder bed fusion additive manufacturing of metals; physics, computational, and materials challenges. Appl. Phys. Rev. 2, 041304. https://doi.org/10.1063/1.4937809

Lee, Y., Nordin, M., Babu, S.S., Farson, D.F., 2014. Effect of fluid convection on dendrite arm spacing in laser deposition. Metall. Mater. Trans. B Process Metall. Mater. Process. Sci. 45, 1520–1529. https://doi.org/10.1007/s11663-014-0054-7

Liu, B., Wildman, R., Tuck, C., Ashcroft, I., Hague, R., 2011. Investigation the effect of particle size distribution on processing parameters optimisation in selective laser melting process, in: Solid Freeform Fabrication Symposium. Austin, TX.

Lumay, G., Boschini, F., Traina, K., Bontempi, S., Remy, J.C., Cloots, R., Vandewalle, N., 2012. Measuring the flowing properties of powders and grains. Powder Technol. 224, 19–27. https://doi.org/10.1016/j.powtec.2012.02.015

Ngo, T.D., Kashani, A., Imbalzano, G., Nguyen, K.T.Q., Hui, D., 2018. Additive manufacturing (3D printing): A review of materials, methods, applications and challenges. Compos. Part B Eng. 143, 172–196. https://doi.org/10.1016/j.compositesb.2018.02.012

Rubenchik, A.M., King, W.E., Wu, S.S., 2018. Scaling laws for the additive manufacturing. J. Mater. Process. Technol. 257, 234–243. https://doi.org/10.1016/j.jmatprotec.2018.02.034

Sames, W.J., List, F.A., Pannala, S., Dehoff, R.R., Babu, S.S., 2016. The metallurgy and processing science of metal additive manufacturing. Int. Mater. Rev. 61, 315–360. https://doi.org/10.1080/09506608.2015.1116649

Spierings, A.B., Herres, N., Levy, G., 2011. Influence of the particle size distribution on surface quality and mechanical properties in AM steel parts. Rapid Prototyp. J. 17, 195–202. https://doi.org/10.1108/13552541111124770

Spierings, A.B., Voegtlin, M., Bauer, T., Wegener, K., 2016. Powder flowability characterisation methodology for powder-bed-based metal additive manufacturing. Prog. Addit. Manuf. 1, 9–20. https://doi.org/10.1007/s40964-015-0001-4

Trapp, J., Rubenchik, A.M., Guss, G., Matthews, M.J., 2017. In situ absorptivity measurements of metallic powders during laser powder-bed fusion additive manufacturing. Appl. Mater. Today 9, 341–349. https://doi.org/10.1016/j.apmt.2017.08.006

Verbelen, L., 2016. Towards scientifically based screening criteria for polymer laser sintering. KU LEUVEN.

Wang, J.-H., Ren, J., Liu, W., Wu, X.-Y., Gao, M.-X., Bai, P.-K., 2018. Effect of Selective Laser Melting Process Parameters on Microstructure and Properties of Co-Cr Alloy. Materials (Basel). 11, 1546. https://doi.org/10.3390/ma11091546

Zhao, C., Zhou, J., Mei, Q., Ren, F., 2019. Microstructure and dry sliding wear behavior of ultra fi ne-grained Co-30 at % Cr alloy at room and elevated temperatures. J. Alloys Compd. 770, 276–284. https://doi.org/10.1016/j.jallcom.2018.08.092

Zhu, H.H., Fuh, J.Y.H., Lu, L., 2007. The influence of powder apparent density on the density in direct laser-sintered metallic parts. Int. J. Mach. Tools Manuf. 47, 294–298. https://doi.org/10.1016/j.ijmachtools.2006.03.019

Conclusion Chapter

The overall conclusion is that there is plenty of research remaining to improve our understanding of laser energy-material interaction. Two examples of such research were reported here, showing clearly that certain laser parameters (i.e. 55 MHz) and materials either perform a useful process (local melting or coalescing tailored particles) and/or provide new transferable knowledge (heat accumulation to anneal or melt over long exposure times). Both chapters study material processing done a remarkably low average powers, 0.3 to 1 W for ultrafast heat accumulation, and 12 W for powder coalescence. In the first chapter, the transferable knowledge gained is that high repetition rate (55 MHz) ultrafast lasers exhibit heat accumulation up to melt ablation over relatively long (>100 millisecond) exposure times, and therefore are not useful for fast removal rates nor clean ablation. The transition away from heat accumulation towards clean ablation should occur near repetition rates that match the thermal diffusion time to the duty cycle of the pulsed laser. For tungsten carbides, that time is estimated to be 3 μs, and ideal ablation removal rates should be explored near the ablation threshold around several hundred kHz. The poorly understood incubation effects are known to be affected by repetition rate (also exposure time and number of pulses for perhaps the first time in this work), pulse energy (thermal penetration depth), thermal conductivity and diffusivity (measured in this work explicitly), temperature dependency of absorption and thermal properties (not often nor easily measured, but important), and scanning speed (for perhaps the first in this work). In the second chapter, the transferable knowledge is a forecasted paradigm shift towards easier qualification and testing of new alloys that can be tailored to the AM process

(rather than tailoring AM process variables to build density or mechanical properties). The rapid thermal heating/cooling during laser AM should allow performance benefits due to fine grained, meta-stable phases introduced during milling powder processing, which still needs further research to clearly demonstrate. The fast thermal laser treatment should allow for process-unique meta-stable microstructure and final printed properties. A second main paradigm shift is towards high throughput qualification and testing by using small batches by ball milling. The spheroidization, size distribution, and powder-fed flow is sufficient and controllable, as shown by (Fullenwider et al., 2019) and others, with ball milling approaches, but the research has generally been limited to one or two (low throughput) alloys or composites per project. Although not reported in detail, stainless 304, 17-4, 316L, pure Fe, pure Ni, pure Cu, pure Ti, Ti-6Al-4V, and Ni-Ti commercial powders as well as custom milled five-element high entropy alloys (x3), Cr-15Ni, Cr-25Ni, and Mg-1.5Ti have been tested for laser coalescence in a small cup with K40 cw-laser raster heating. In the context of ball milling approaches, we also hypothesize milling-induced contamination to be a potential nano-particle or nano-phase strengthening benefit. At best, contamination could instead be applied to almost every AM material to improve hardness and strength. In addition, we provide evidence of differences in phase transformation kinetics and Hall flow between milled and atomized versions of powder compositions, and yet similar laser coalesced densities. Commercial scale multi-layer printing with similar milled powders remains as future work to qualify the approach promoted in this work for lab scale single layer processing.